Journal of Colloid and Interface Science 700 (2025) 138361

Contents lists available at ScienceDirect

Journal of Colloid And Interface Science

journal homepage: www.elsevier.com/locate/jcis

Design and evaluation of plasmonic metal-TiO_2 nanostructures for photocatalytic degradation of BPA as a model pollutant

Špela Slapničar [a], Gregor Žerjav [a], Miklós Németh [b], Janez Zavašnik [c], Albin Pintar [a,*]

[a] Department of Inorganic Chemistry and Technology, National Institute of Chemistry, Hajdrihova 19, SI-1001 Ljubljana, Slovenia
[b] Department of Surface Chemistry and Catalysis, Institute for Energy Security and Environmental Safety, HUN-REN Centre for Energy Research, Konkoly-Thege M. Street 29-33, H-1121 Budapest, Hungary
[c] Gaseous Electronics, Jožef Stefan Institute, Jamova 39, SI-1000 Ljubljana, Slovenia

HIGHLIGHTS

- TiO_2 nanorod based noble metal catalysts were synthesized by wet impregnation.
- Plasmonic Pt, Ag and Au on TiO_2 extended the fluorescence lifetime of catalysts.
- Plasmonic effects enhanced ROS generation under visible-light illumination.
- Superoxide anion radicals played the most significant role in BPA degradation.
- Pt + TiO_2 was the most effective due to the most favourable energy band distribution.

GRAPHICAL ABSTRACT

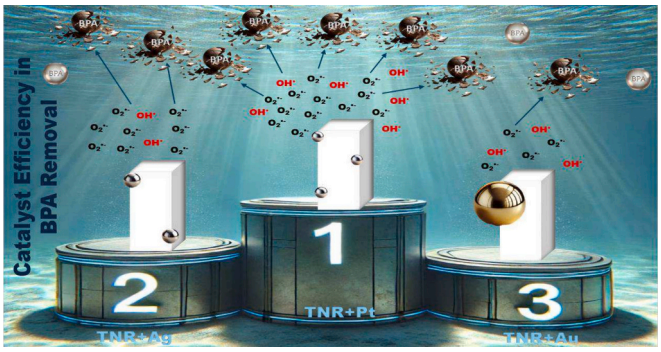

ARTICLE INFO

Keywords:
Heterogeneous photocatalysis
Titanate nanorods
Plasmonic nanoparticles
Wet impregnation
Localized surface plasmon resonance effect

ABSTRACT

This study investigates the improvement of the photocatalytic activity of TiO_2-based catalysts modified with plasmonic metal nanoparticles (PM). Gold (Au), silver (Ag) and platinum (Pt) nanoparticles were uniformly deposited on TiO_2 nanorods (TNR) by a wet impregnation method, achieving a uniform metal loading of 1.0 wt %, which was confirmed by SEM-EDXS analysis. The size of the metallic particles varied, with Pt being the smallest (1.5 nm) and Au the largest (45 nm), while all exhibited a uniform distribution over the TiO_2 surface. The size of the PM nanoparticles was influenced by the pH of the precursor solutions and the isoelectric point of the TNR support. Photoluminescence (PL) measurements showed that TNR-Pt exhibited the lowest charge carrier recombination rate and the highest photocatalytic performance. Tests with reactive oxygen species (ROS) under visible-light exposure showed that TNR-Pt generated the most superoxide anion ($O_2^{\bullet-}$) and hydroxyl ($OH^{\bullet}$) radicals and achieved the highest degradation rate of bisphenol A (BPA). In contrast, TNR-Au showed the lowest ROS formation and BPA conversion rate. The superior performance of the TNR-Pt photocatalyst is attributed to its energy band distribution, which accelerates the oxygen reduction reaction. The results show that $O_2^{\bullet-}$ are the primary reactive species responsible for the degradation of BPA, with the small size of Pt nanoparticles

* Corresponding author.
E-mail address: albin.pintar@ki.si (A. Pintar).

https://doi.org/10.1016/j.jcis.2025.138361
Received 22 May 2025; Received in revised form 4 July 2025; Accepted 5 July 2025
Available online 7 July 2025

promoting ROS production and pollutant degradation, making TNR-Pt the most effective catalyst among the solids investigated in this study.

1. Introduction

Industrial development, population growth and climate change are among the main reasons for the increased consumption of drinking water. In particular, the development of industry and the increase in agricultural activities are linked to the discharge of large quantities of pollutants into the Earth's water. One of the most widespread pollutants in the environment is bisphenol A (BPA) [1–3]. Every year, several million tons of bisphenol waste are produced worldwide [1,4]. BPA is known as an endocrine disruptor [5,6] and is commonly used in the production of polycarbonate plastics used as food and beverage packaging [7]. BPA is an antioxidant that is non-biodegradable and highly resistant to chemical degradation [8]. Even a very low concentration of BPA ($<10^{-12}$ mol/L) can have negative consequences for human health [9]. From 2010 to 2022, the average BPA concentration in European freshwater was reported to be approximately 36 ng/L [10]. In a study by Tappert et al. [11], BPA concentrations in wastewater treatment plant influents in Germany ranged from 0.33 to 910 μg/L, while significantly lower values were observed in effluents. Even higher BPA concentrations, up to 17.2 mg/L, were found in landfill leachates [12,13]. This emphasizes the urgent need for effective BPA removal strategies to protect the environment and human health.

One of the promising approaches for the BPA degradation are advanced oxidation processes (AOPs), which have attracted considerable interest due to their high efficiency [14]. A common feature of AOPs is the formation of extremely reactive, non-selective hydroxyl radicals ($OH^{\bullet}$) [14,15]. These radicals are among the most powerful oxidizing agents used in wastewater treatment [16], as they react immediately and indiscriminately with a variety of organic pollutants. Among the AOPs, the heterogeneous photocatalytic process stands out for its effectiveness [17]. It can be carried out under mild operating conditions, provided that the photocatalyst is stable, inexpensive and photoactive. Among the suitable candidates is TiO_2, which is one of the most frequently investigated semiconductors for use in the process of heterogeneous photocatalytic oxidation of pollutants in water due to its good properties. Despite all the advantages that TiO_2 has, there are also some disadvantages, such as a large band gap and rapid recombination of the electron-hole pairs (e^--h^+) [18]. The solution is to form a heterojunction between TiO_2 and the plasmonic metal, which can prevent the recombination of the e^--h^+ pairs. These metals enhance light absorption in the visible region via surface plasmon resonance and promote more efficient charge separation, thereby improving the overall photocatalytic activity [19]. Selected plasmonic nanoparticles (Au, Ag and Pt) are considered very interesting for use in various fields, such as medicine, biotechnology and also catalysis, with unique properties [20]. Gold nanoparticles are known as stable, non-toxic particles [21,22], which are often used for application on TiO_2 semiconductor to improve the catalytic properties and activity of the material. Platinum nanoparticles have a large surface area, which increases catalytic activity, while their stability in different environments ensures durability during reactions [23]. We also opted for silver nanoparticles mainly because of their low cost [24]. The choice of plasmonic metal is important because the activity of the synthesized catalyst depends on it. However, it should be noted that different plasmonic metals also have a different tendency to form clusters of different sizes [25].

The size of plasmonic nanoparticles has a significant impact on their catalytic activity, mainly through their optical properties and the generation of hot electrons. Research shows that both the absorption and scattering properties of these nanoparticles are size-dependent, which affects their efficiency in photocatalytic reactions. Smaller nanoparticles tend to generate hot electrons more efficiently, which are crucial for driving chemical reactions [26]. For example, smaller Ag nanoparticles (6 nm) showed better photocatalytic activity than their larger counterparts due to enhanced hot electron generation [26]. Conversely, larger Au@Pd NPs (up to 120 nm) showed better catalytic performance under certain conditions, e.g. at elevated temperature, due to improved photon utilization through scattering effects [27]. While smaller nanoparticles are often favoured due to their generation of hot electrons, larger nanoparticles can also be effective under certain conditions. This suggests that the optimal size for catalytic activity may vary depending on the specific reaction and environmental factors.

Plasmonic metal-based TiO_2 materials are widely used in photocatalytic applications, especially in wastewater treatment. However, previous research on BPA degradation has mainly focused on TiO_2-Au materials. Studies by Hidayat et al. [28] and Cao et al. [29] have also investigated the potential of TiO_2-Ag and TiO_2-Pt solid samples for photocatalysis, but with high catalyst concentration in the reaction mixture, which may hinder practical applications. This challenge motivated our current study, in which we attempted to use lower catalyst concentrations and still achieve effective BPA degradation. To better understand the influence of the different metals on TiO_2, we conducted a systematic study and synthesized the catalysts using a simple wet impregnation method.

In this study, we aimed to develop and evaluate plasmonic metal-TiO_2 nanostructures (TNR-Au, TNR-Ag, TNR-Pt) for the photocatalytic degradation of BPA under visible light. The catalysts were synthesized using a simple wet impregnation method and thoroughly characterized for their morphological, surface, optical, and electronic properties. Considering the global problem of BPA pollution, we focused on the degradation of BPA, a persistent organic pollutant, under visible light illumination using catalysts with lower concentrations. By directly comparing the influence of different plasmonic metals, this work provides valuable insights into their role in enhancing the photocatalytic degradation of BPA and contributes to the development of more effective materials for sustainable water treatment.

2. Experimental

2.1. Materials

Sodium hydroxide (NaOH, ≥98 %, Merck), hydrochloric acid (HCl, fuming 37 %, ≤1 ppm free chlorine, Merck), gold (III) chloride hydrate ($HAuCl_4 \cdot xH_2O$, ~50 % Au basis, Sigma Aldrich), diamminedinitritoplatinum (II) solution ($Pt(NH_3)_2(NO_2)_2$, 3.4 wt% in dilute ammonium hydroxide, Sigma Aldrich), silver nitrate ($AgNO_3$, ≥99.8 %, Kemika), absolute ethanol (C_2H_5OH, ≥99.5 %, Carlo Erba reagents), coumarin (COUM, ≥98 %, Thermo Fisher), 1,1-diphenyl-2-picrylhydrazyl (DPPH, Sigma Aldrich), 2,2′-azino-bis-(3-ethylbenzothiazoline-6-sulfonic acid) cation ($ABTS^{\bullet+}$, ≥98 %, Sigma Aldrich), potassium persulfate ($K_2S_2O_8$, ≥99 %, Sigma Aldrich), and bisphenol A (BPA, ≥99 %, Sigma Aldrich) were used as received. TiO_2 precursor DT-51 was donated from the company CristalACTiV™ (Tronox, UK). All aqueous solutions used in this work were prepared with ultrapure water (18.2 MΩ cm, PURELAB Flex, ELGA LabWater, UK) and kept in the dark at 4 °C.

2.2. Catalyst synthesis

Titanate nanorods (TNR) were synthesized via hydrothermal synthesis [30]. In brief, 2 g of a commercial TiO_2 precursor (DT-51, CristalACTiV™), consisting of more than 99 wt% anatase TiO_2, was dispersed in an aqueous sodium hydroxide solution (10 M). The mixture

was transferred into a Teflon-lined autoclave and maintained at 130 °C for 24 h. After cooling, the resulting precipitate was separated by centrifugation at 600 rpm and washed thoroughly several times with 0.1 M HCl and ultrapure water until neutral pH was reached. The purified material was then calcined at 500 °C for 2 h in air, using a heating ramp of 120 °C per hour, to obtain the final TNR product.

Plasmonic metal (PM) nanoparticles were deposited on the TNR surface using a modified wet impregnation technique based on our previously reported procedure [31]. The TNR support was ultrasonically dispersed in ethanol for 10 min. To this suspension, one of the following metal precursor solutions was added: (i) 10 mM $HAuCl_4$, (ii) 10 mM $AgNO_3$ aqueous solution, or (iii) 3.4 wt% $Pt(NH_3)_2(NO_2)_2$ solution in dilute ammonium hydroxide. The amount of precursor was adjusted to achieve a nominal metal loading of 1.0 wt%. The mixture was magnetically stirred continuously at 400 rpm for 2 h, after which the solvent was removed by rotary evaporation and dried at 80 °C for 18 h. The final calcination was carried out at 300 °C for 2 h in a 5 % H_2/95 % N_2 gas mixture with a heating ramp of 150 °C per hour [32]. The prepared TiO_2-PM catalysts were TNR with gold nanoparticles (referred as TNR-Au), TNR with silver nanoparticles (referred as TNR-Ag) and TNR with platinum nanoparticles (referred as TNR-Pt). The materials were calcined using a Nabertherm chamber furnace (Germany, model LV 5/11/P330).

2.3. Catalyst characterization

The measurements of N_2-physisorption were carried out with a Micromeritics TriStar II 3020 analyzer. Prior to the measurements, the catalysts were degassed with N_2 (Messer, purity 6.0) using a Micromeritics SmartPrep unit, first at 90 °C for 1 h, then at 180 °C for 4 h. The Brunauer-Emmett-Teller (BET) method was used to determine the specific surface area, while the pore volume and pore size distribution were determined from the desorption isotherms using the Barrett-Joyner-Halenda (BJH) method. The crystallinity and phase composition of the synthesized catalysts were investigated by powder X-ray diffraction (XRD) analysis using a PANalytical X'Pert Pro diffractometer with Cu Kα1 radiation (λ = 0.15406 nm). Scanning was performed in the 2θ range between 5 and 90°, with a step size of 0.033° and a step time of 100 s.

Morphological and compositional analyzes were performed using the transmission electron microscope (TEM, JEM-2100, JEOL Inc.) and the scanning electron microscope (SEM, SUPRA 35 VP, Carl Zeiss) equipped with an energy-dispersive X-ray spectrometer (EDXS, Inca 400, Oxford Instruments). For TEM analysis, the samples were ultrasonically dispersed in ethanol and applied to amorphous carbon support grids. For SEM-EDXS analysis, the powdered catalysts were attached to an aluminium holder with double-sided adhesive tape and then carefully purged with a stream of air to remove the residual amount of samples that were not attached to the carbon tape.

Zeta potential measurements of the tested materials were performed at 25 °C using a Malvern Panalytical Zetasizer (model Ultra Red) equipped with ZS EXPLORER software and a multipurpose titrator (MPT-3). The pH of the suspensions was adjusted between 2 and 9 using 0.25 M sodium hydroxide (NaOH) and 0.25 M/0.025 M hydrochloric acid (HCl) aqueous solutions.

The UV–Vis diffuse reflectance spectra (UV–Vis DR) of the analyzed catalysts were recorded in the range of 200 to 900 nm using a UV–Vis spectrophotometer (Perkin Elmer, model Lambda 650) equipped with a Praying Mantis DRP-SAP accessory from Harrick. The scan rate was set to 266.75 nm per minute and measurements were performed at room temperature. Photoluminescence (PL) measurements of solid samples were performed using a Perkin Elmer LS 55 UV–Vis fluorescence spectrometer. The excitation wavelength was 300 nm, the excitation slit was 5 nm, the emission slit was 7.5 nm and the scan speed was set to 200 nm per minute over a wavelength range of 300 to 600 nm. A spectrofluorometer (Horiba, model Fluorolog-QM 75–22) equipped with a picosecond photon detector (Horiba, model PPD 850) was used for time-correlated single photon counting (TCSPC). The width of the excitation and emission slit was set to 8 nm and a DeltaDiode pulsed laser source with an excitation wavelength of 495 nm was used (Fig. S1). The response was measured at emissions of 350, 520, 550 and 600 nm. A Ludox SM-30 colloidal silica solution was used as a reference to determine the instrument response function (IRF), which was used to calculate the lifetimes of the charge carriers using the FelixFL spectroscopy software. The Ludox solution is ideally suited for this purpose due to its rapid light scattering and negligible fluorescence and ensures accurate measurement of the system's response over time.

X-ray photoelectron spectroscopy (XPS) was used to analyze the composition and chemical state of the sample surfaces. For this purpose, a Thermo Scientific ESCALAB Xi+ instrument with a monochromatized Al K-alpha source (1486.6 eV) with a spot size of 650 μm was used. For each sample, broadband spectra (at an analyzer pass energy of 80 eV) were collected for each sample to determine the elemental composition. For quantitative and chemical state analysis, high-resolution spectra (at a pass energy of 20 eV) were collected for the following photoelectron lines: C 1 s, O 1 s, Ti 2p, Ag 3d, Au 4f, Pt 4f and valence band regions. The charging of the sample surface was compensated using the automatic charge equalization system built into the device. The maximum of the Ti $2p_{3/2}$ peak at 458.7 eV was used as an internal reference for fine adjustment of the energy scale. A Shirley baseline was used to determine the peak areas. In the case of Au 4f and Pt 4f, the background of the metal-free TNR sample was subtracted from the spectra. The ratio of the elements was calculated from the integral intensities of the XPS lines using the sensitivity factors specified by the manufacturer. The errors in the quantitative analysis (elemental composition) were estimated in the range of ±10 %. All spectra were processed using Avantage software, including determination of valence band maxima (VBM).

2.4. Evaluation of the photocatalytic activity

To evaluate the generation of reactive oxygen species (ROS) under visible light, three different probe reactions were used: (i) a 200 mg/L aqueous solution of coumarin (COUM) was used as a probe, with the formation of 7-hydroxycoumarin (7-OHC) indicating the presence of $OH^\bullet$ radicals [33], (ii) a 40 μM solution of (2,2-diphenyl-1-picrylhydrazyl) (DPPH) in water:ethanol mixture (1,1, *v*/v) to monitor the e^-, h^+, $OH^\bullet$ and $O_2^{\bullet-}$ species [34–37], and (iii) an aqueous solution of $ABTS^{\bullet+}$ prepared by dissolving 17.2 mg of 2,2′-azino-bis(3-ethylbenzothiazoline-6-sulphonic acid) salt ($ABTS^{\bullet+}$) and 3.3 mg of $K_2S_2O_8$ in 5 mL of ultrapure water to monitor e^- and $O_2^{\bullet-}$ production [36].

For the COUM-based reaction, 10 mg of the prepared catalysts were added to 50 mL of the COUM solution in a 100 mL glass batch reactor. The suspension was magnetically stirred at 400 rpm and allowed to stand in the dark for 20 min to establish adsorption equilibrium. The mixture was then externally irradiated using a Schott KL 2500 LED (Germany) visible light source. Aliquots were taken at specific time intervals, filtered with a 0.2 μm membrane filter and analyzed with a Perkin Elmer LS 55 UV–Vis photoluminescence spectrometer in a 10 × 10 mm quartz cuvette. The excitation wavelength was set to 338 nm, the excitation and emission slits to 10 nm and the scan speed to 200 nm per minute. The intensity of the photoluminescence of the produced 7-OHC was measured at λ = 456 nm [33].

For the DPPH assay, only 1 mg of the catalyst was suspended in 50 mL of DPPH solution under the same illumination and mixing conditions. The changes in DPPH concentration over time were monitored by UV–Vis spectra (Perkin Elmer, model Lambda 465) using a quartz cuvette with an optical path length of 10 mm; for quantitative purposes, the absorbances at the peak maxima at λ = 523 nm were considered [37].

For the $ABTS^{\bullet+}$ measurements, 1 mL of the prepared stock solution was diluted with 50 mL of ultrapure water. The absorbance changes at 415 and 340 nm were monitored with a TrayCell cuvette (Hellma,

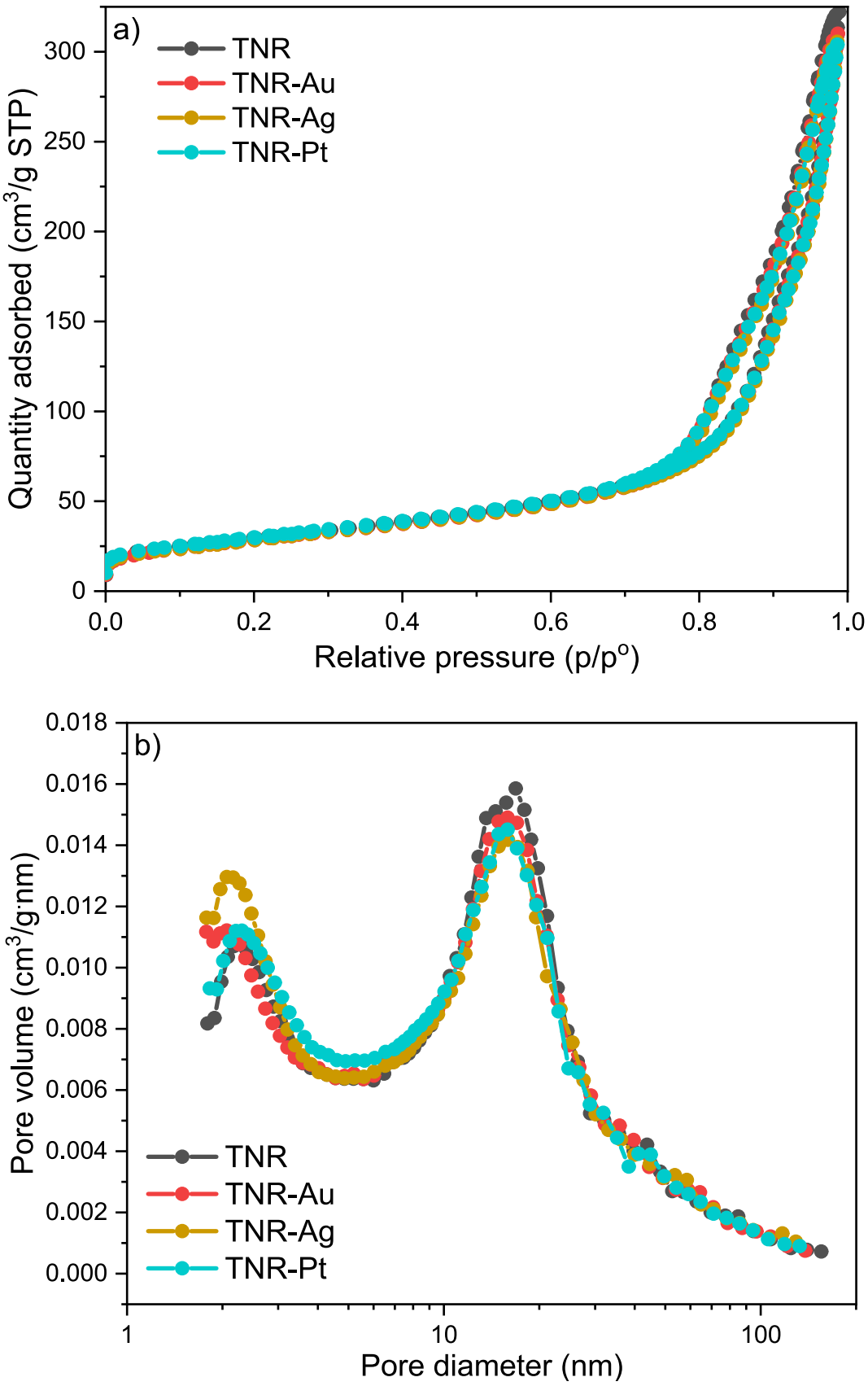

Fig. 1. a) Nitrogen adsorption/desorption isotherms of the TNR support and the catalysts TNR-Au, TNR-Ag and TNR-Pt; b) corresponding BJH pore size distribution.

Table 1
Comparison of N_2 physisorption (specific surface area (S_{BET}), total pore volume (V_{pore}) and average pore diameter (d_{pore})), XRD and SBH results. The apparent crystallite size of anatase was calculated using the Scherrer equation from the diffraction peaks at 25°.

Sample	TNR	TNR-Au	TNR-Ag	TNR-Pt
S_{BET} (m^2/g)	106	105	106	108
V_{pore} (cm^3/g)	0.48	0.47	0.48	0.47
d_{pore} (nm)	18.3	17.9	17.4	17.1
Apparent anatase crystallite size (nm)	17.4	17.4	17.4	17.4
Average metal nanoparticles size (nm)	–	45	5	1.5
SBH (eV)	–	0.09	0.11	0.14

dilution factor 5, light path 2 mm) by recording UV–Vis spectra [36]. The experimental setup and operating conditions for the measurements were the same as for the two previous experiments.

To evaluate the photocatalytic degradation of bisphenol A (BPA), a model organic pollutant, a 10 mg/L BPA solution was prepared (initial pH_{BPA} = 6.1). Physicochemical properties of BPA are listed in Supplementary information. The experiments were performed in a batch glass slurry reactor (Lenz Laborglas, model LF60) at a constant temperature of 25 °C (Julabo, model F25/ME) and atmospheric pressure. The suspension contained 125 mg/L catalyst with 250 mL of BPA and was magnetically stirred at 600 rpm, with a continuous air supply of 750 mL/min. After 30 min of dark equilibration, visible light (halogen lamp, Philips, 150 W, λ_{max} = 520 nm, irradiation flux equal to 0.53 W/cm^2) was used. The energy spectra of the light sources used are shown in Fig. S1 of the Supplementary information. The collected liquid-phase samples were filtered through a 0.2 μm membrane filter and analyzed for temporal BPA concentration using an HPLC instrument (Shimadzu, model LC-40) in isocratic mode. The column (100 × 4.6 mm BDS Hypersil C18 (2.4 μm)) was thermostated at 30 °C. The mobile phase consisted of a mixture of methanol and ultrapure water (70 %, 30 %, *v*/v) at a flow rate of 0.5 mL/min. Detection was performed with a PDA detector in the wavelength range between 190 and 350 nm. The instrument was calibrated daily in the range of 0–20 mg/L BPA using reference solutions. At the end of the photocatalytic oxidation of BPA, the total organic carbon (TOC) content was measured using a Shimadzu TOC-L CPH/CPN analyzer (calibrated routinely in the range of 0.1–10 mg/L C) to determine the extent of mineralization of BPA.

To ensure the reliability and reproducibility of our photocatalytic results, all experiments were performed in triplicate.

3. Results and discussion

3.1. Structural properties of the catalysts

Information on the specific surface area (S_{BET}), the total pore volume (V_{pore}) and the average pore diameter (d_{pore}) of the analyzed materials was obtained by N_2 physisorption (see Fig. 1 and Table 1). Table 1 shows

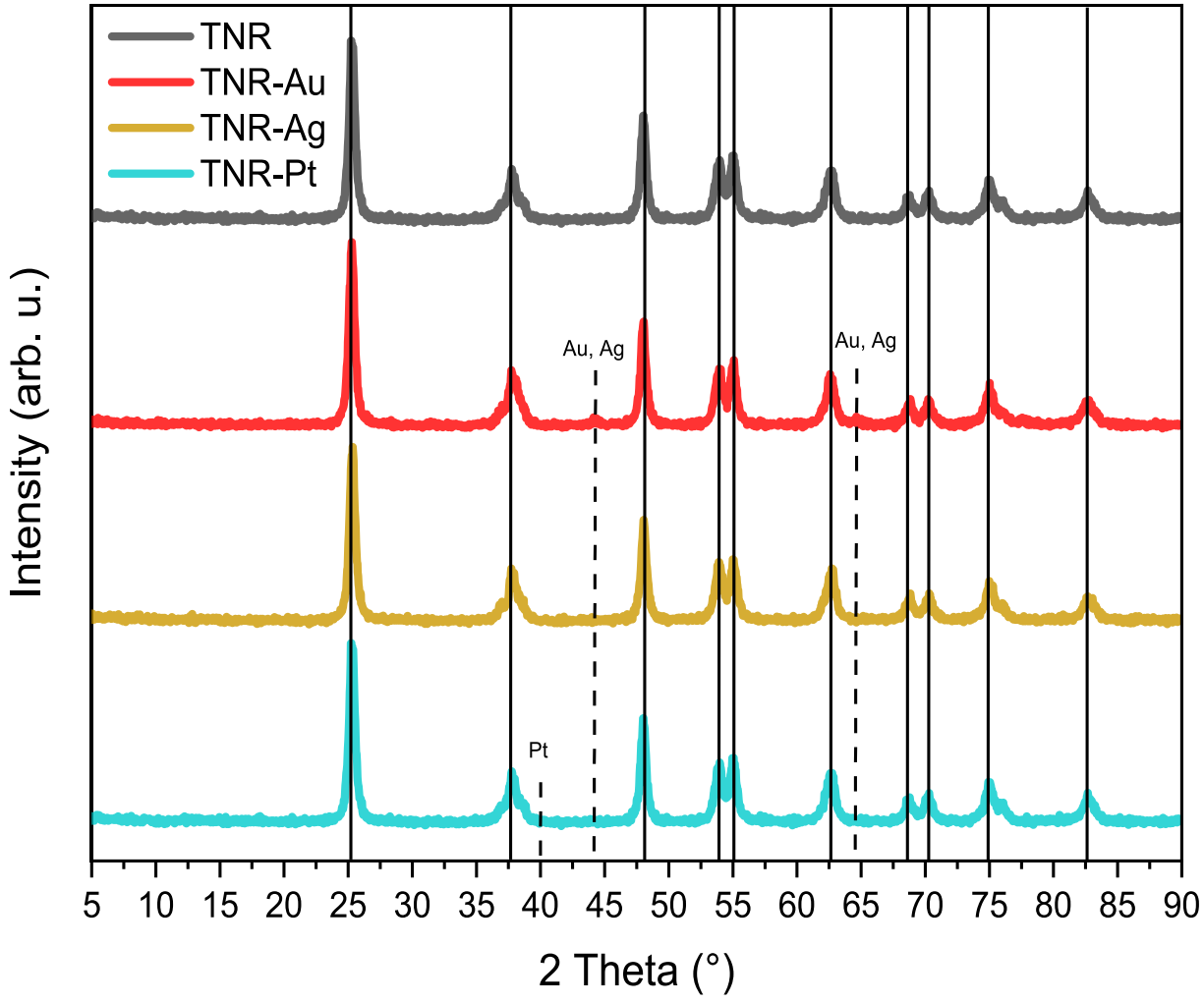

Fig. 2. XRD diffractograms of the TNR support and the TNR-PM photocatalysts. The solid vertical lines belong to anatase TiO_2 (JCPDS 00-021-1272) and the dotted lines to the plasmonic metals.

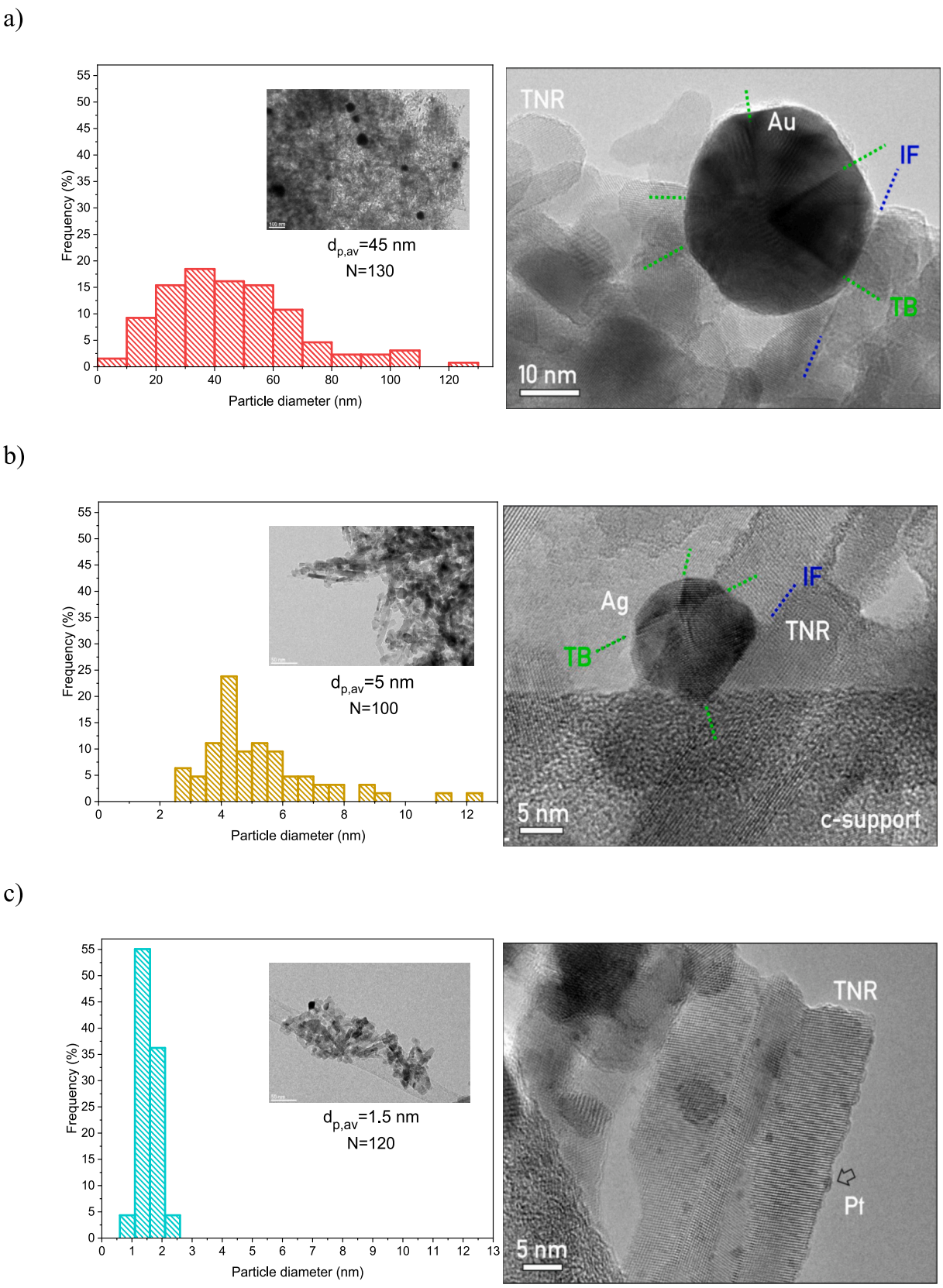

Fig. 3. Particle size distribution of the PM clusters of the prepared TNR-PM catalysts and HR-TEM results of a) TNR-Au, b) TNR-Ag and c) TNR-Pt. The NP size was calculated using the Image J program.

Table 2
Results of SEM-EDXS elemental analysis of the TNR and TNR-PM catalysts.

Sample		TNR	TNR-Au	TNR-Ag	TNR-Pt
Ti	wt%	49.8 ± 2.0	53.5 ± 2.1	54.7 ± 3.3	51.9 ± 3.0
O		50.2 ± 2.0	45.7 ± 2.1	44.3 ± 3.3	47.1 ± 3.0
Au		–	0.8 ± 0.1	–	–
Ag		–	–	1.0 ± 0.1	–
Pt		–	–	–	1.0 ± 0.1

that the obtained values were the same for all investigated materials, which is a first indication that the deposited PM were deposited on the surface of the TNR support and thus the morphological properties of the investigated solids are mainly dominated by the properties of the TNR. Due to the nature of TiO_2, the porosity measured in the samples is most likely interparticle rather than intraparticle pores [38]. The prepared catalysts exhibit N_2 adsorption-desorption isotherms corresponding to the type IV isotherm according to the IUPAC classification [39], which places them among the mesoporous materials with pore sizes ranging from 2 to 50 nm. The typical curve shape at $p/p^o = 1$ indicates that the catalysts also contain pores with a size of more than 50 nm, i.e. macropores [40].

The XRD diffractograms of the analyzed materials are illustrated in Fig. 2 and show the same profile, regardless of whether and which PM was deposited. The expressed peaks are characteristic of the anatase form of TiO_2, leading to the conclusion that the synthesized TNR support consists only of the crystalline anatase phase. Since the Scherrer equation is used to calculate the crystallite size of spherical particles (by calculating the volume of the single crystallite) and the TiO_2 synthesized in this study was in the form of nanorods, we can only estimate the apparent size of the anatase crystallites using the XRD technique (Table 1). The average apparent size of the TiO_2 anatase crystallites was 17 nm for all materials analyzed. This confirms the results of the N_2 physisorption analysis, from which we concluded that the PM were deposited only on the surface of the TNR support. Small peaks were visible for the Au-doped catalyst, probably because the Au nanoparticles were larger and their crystallites were easier to observe with XRD analysis and their size were 9 nm. Peaks for Ag and Pt were not visible in the XRD diffractograms because the contents of the plasmonic metals were below the detection limit of the XRD analysis [41]. Furthermore, the absence of Ag/Pt XRD peaks can be attributed to the good distribution of the PM particles over the TNR surface and/or the small size of the PM particles obtained.

Using TEM analysis, we were able to view microscopic images of the synthesized TNR and TNR-PM catalysts (see inset in Fig. 3). The technique confirmed that the TNR were indeed defined nanorods with a uniform size of 80 nm in length and 8 nm in width (measured on TEM micrographs, not shown here). The plasmonic metals were uniformly distributed over the TNR catalyst support and their morphology was almost spherical. The size difference between the individual metals was large, as the Au aggregates were much larger than the Ag and Pt nanoparticles (Fig. 3, Table 1). Especially for the latter, it is known that its particles are always up to 5 nm in size [42,43], which was also

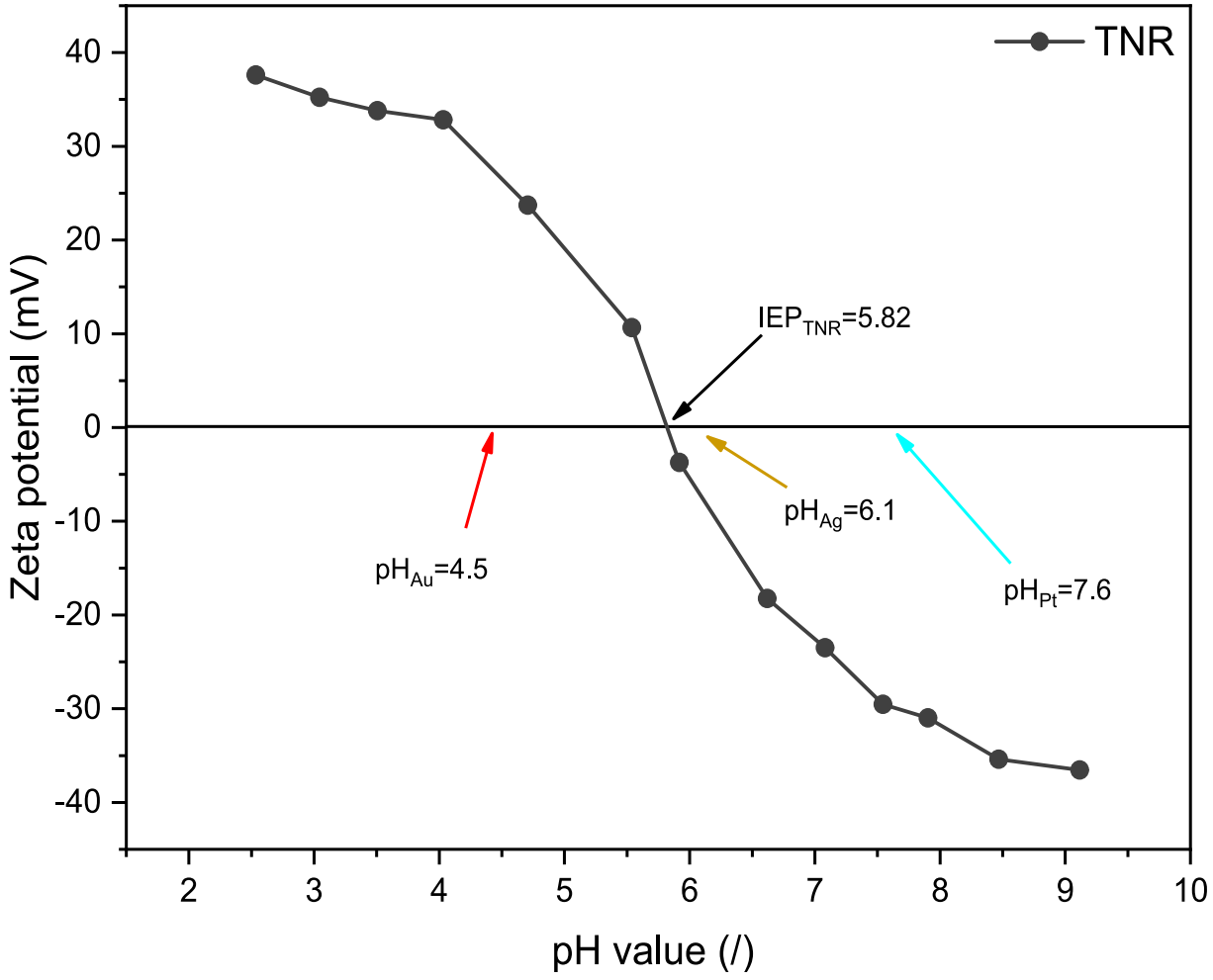

Fig. 4. The change in zeta potential as a function of the pH value of the suspension for the TNR support. The zeta potential decreases with increasing pH between 40 mV and − 40 mV. The pH values of the precursor solutions are also labelled.

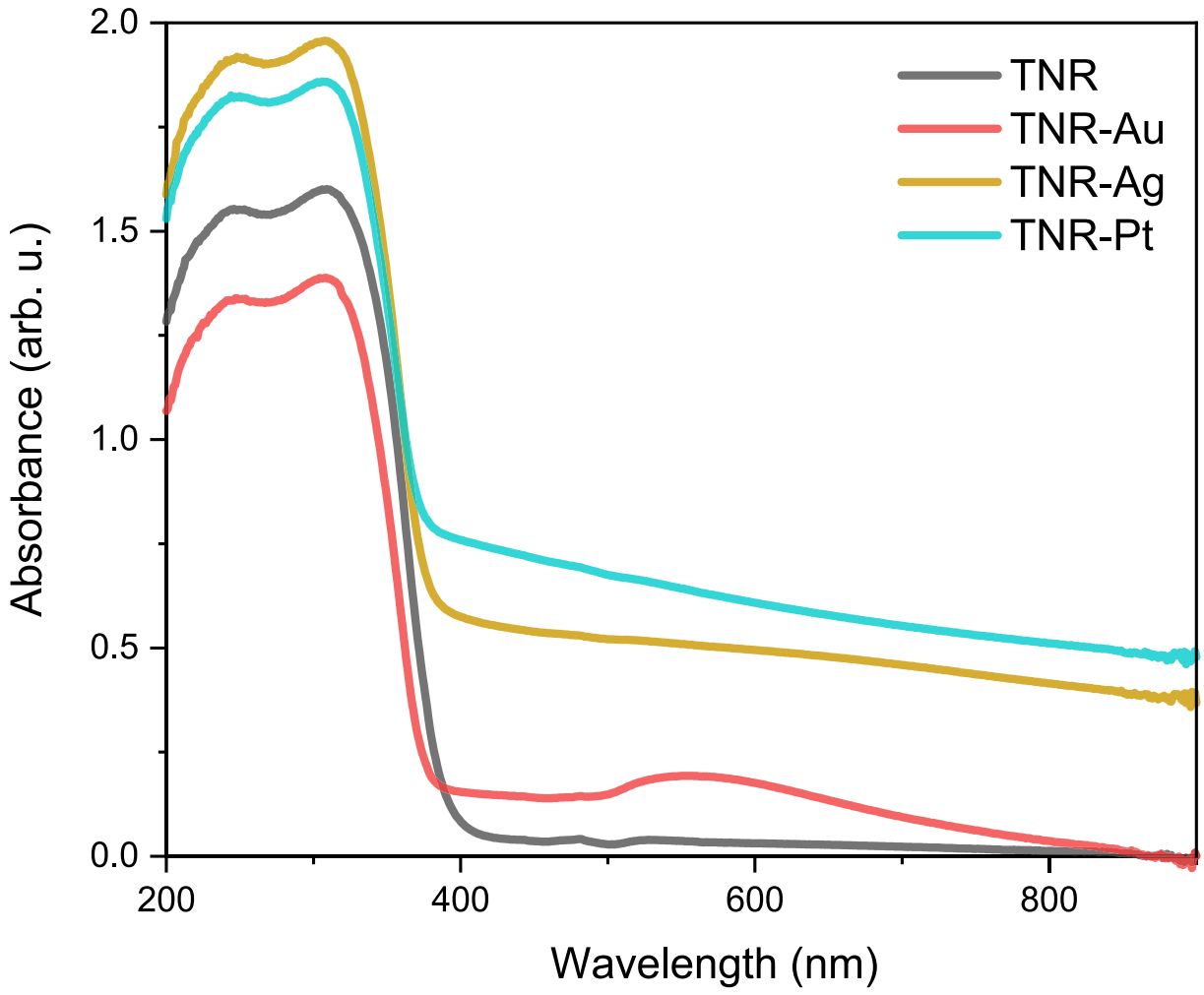

Fig. 5. UV–Vis DR spectra of the TNR support and the catalysts with 1.0 wt% PM.

confirmed in our study (see average particle size in Table 1). The particle size distribution of Au-NP in the prepared TNR-Au sample was broader, and several of the measured Au nanoparticles were larger than 100 nm. In contrast, the size distribution of Ag and Pt particles was extremely narrow. Au nanoparticles usually have a larger diameter, which was also observed by Verma et al. [32]. High-resolution TEM (HR-TEM) images (Fig. 3) reveal a clear interface (IF) between TiO_2 and the deposited metal nanoparticles, confirming the formation of a heterojunction. Additionally, the presence of twin boundaries (TB) in the metallic domains indicates a high crystallinity and a potential influence on electron transport or catalytic activity. Despite the different sizes of the plasmonic particles on the TNR support, the final conclusions remained similar or identical (see Supplementary information). Finally, the results of the SEM-EDXS analysis showed that the loading of the plasmonic metals was 1.0 wt%, which corresponded to the nominal loading. The experimentally measured contents of Ti, O and Au/Ag/Pt are listed in Table 2. Fig. S2 illustrates the spatial distribution of these elements in the synthesized catalysts.

The zeta potential as a function of pH was measured for the TNR catalyst support. As the pH value increases, the zeta potential decreases, as can also be seen in Fig. 4. The isoelectric point (IEP) is the pH of the suspension at which the net charge of a catalyst surface becomes zero. The IEP of TNR was measured to be 5.82, which is close to the literature data (6.0 for anatase TiO_2 [44,45]). The solutions of the precursors have different pH, which affects the size distribution of PM particles on the TNR surface. The solution of the Au precursor had a lower pH than the IEP of TNR and the Pt precursor had a higher pH. The pH of the Ag precursor solution was close to the IEP of TNR. The literature states that the pH of the precursor solutions is very important as a pH below the IEP leads to larger metal particles on the TNR surface and vice versa. The same trend was seen in our samples, as the largest metal clusters were formed by Au (average 45 nm), whose precursor solution had an acidic pH, while the pH of the Pt precursor solution was basic and the resulting particles were the smallest (average 1.5 nm).

3.2. *Chemical and optoelectronic properties of the catalysts*

The UV–Vis DR spectra for TNR-PM catalysts are shown in Fig. 5. The spectra show light absorption in the UV and visible range. The light absorption below 400 nm was attributed to the presence of TiO_2 in the samples. In the TNR-Au sample, a hump is visible at a wavelength of 550 nm, which is due to the LSPR effect expressed by the plasmonic properties of the Au nanoparticles. According to the literature [46], the LSPR effect of Ag particles with a diameter of less than 10 nm occurs at a wavelength of about 400 nm. In our case, the hump in the TNR-Ag sample is not visible in the visible range, as the average Ag diameter is also less than 10 nm (5 nm on average). Interestingly, the TNR-Pt and TNR-Ag samples have a higher absorption in the visible-light range. Electronic excitations from filled s-states below the Fermi level to empty states above the Fermi level are possible and are referred to as intraband transitions [47]. The band gap for the TNR sample is 3.2 eV, which agrees with the values given in the literature for anatase TiO_2 [48,49].

The charge carriers generated in a photocatalyst can be used, for example, for the generation of ROS and so on. However, if they are not

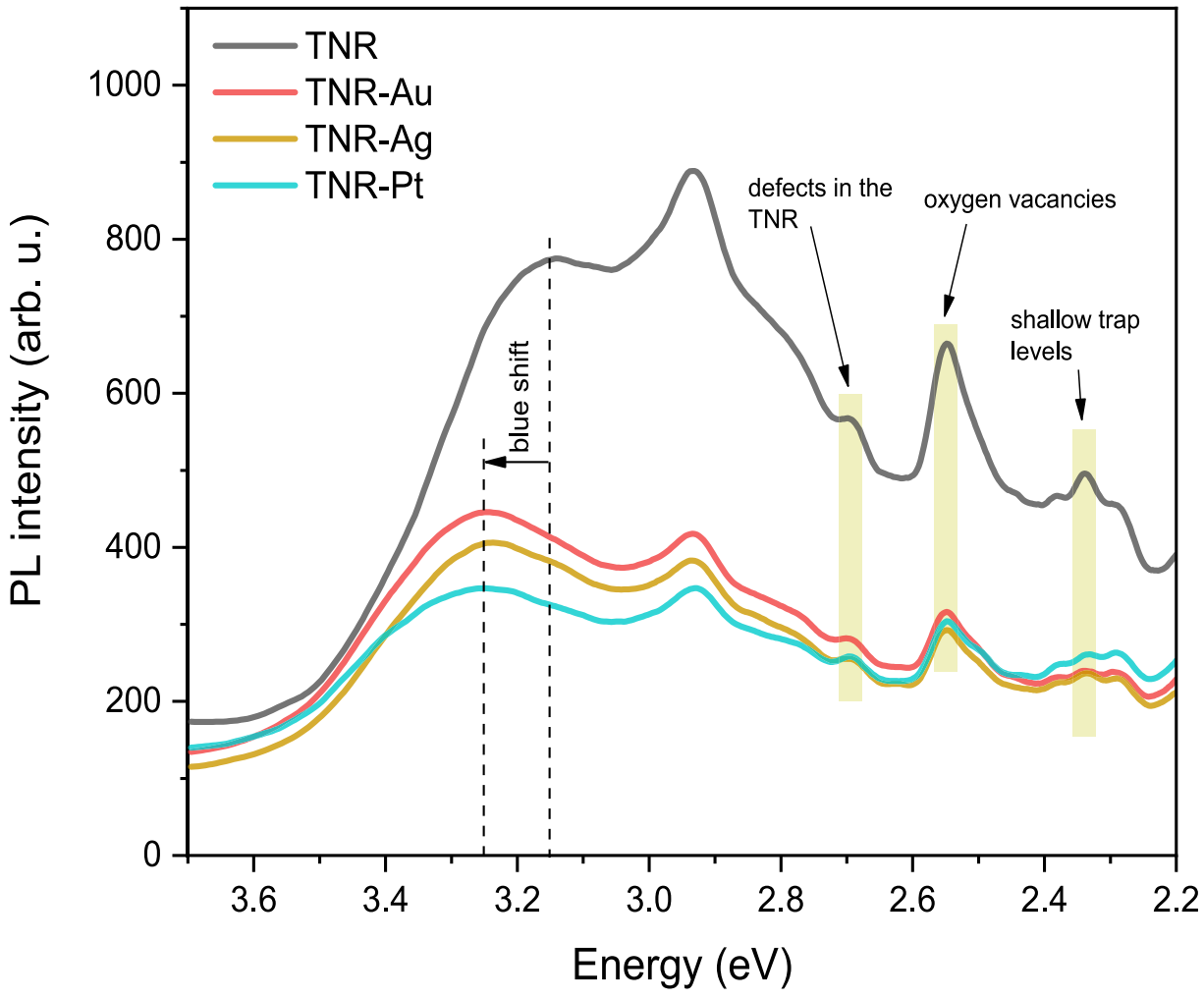

Fig. 6. Photoluminescence (PL) solid-state spectra of the catalysts investigated.

consumed in any of the reactions, they tend to recombine and generate energy in the form of photoluminescence. A high PL intensity in the solid-state PL curves of a photocatalyst is an indication of a high charge carrier recombination rate of the photocatalyst under investigation. This is a known disadvantage of TiO_2-based photocatalysts in particular. The addition of PM to TiO_2 should reduce the PL intensity, as the recombination of charge carriers should be hindered by the migration of charge carriers between TiO_2 and PM. Fig. 6 shows the solid-state PL spectra of the materials we analyzed. The peak at 3.15 eV in the PL spectrum of the bare TNR is characteristic of the anatase TiO_2 [50]. For the TNR-PM catalysts, a blue shift was observed in the range from 3.15 eV to 3.25 eV, which is due to the fact that the metal ensembles selectively suppress phonon-assisted indirect transitions in anatase TiO_2 [51]. The peak at an energy of 2.9 eV indicates the lowest indirect transition $\Gamma_{1b} \rightarrow X_{1a}$. The peaks in the PL spectra between 2.7 and 2.3 eV are characteristic of defects in the TNR carrier, oxygen vacancies and shallow trap levels (labelled in Fig. 6). The results of the PL measurements for the samples with the addition of plasmonic nanoparticles show a lower intensity as there is less emitting recombination in the samples. This improvement contributes to an improved photocatalytic activity of the TNR-PM photocatalysts compared to pure TNR (see below).

The results of the fluorescence lifetime are shown in Fig. 7. The measurements were performed with a TCSPC setup in which the excitation/emission process was repeated 10,000 times to create a histogram of photon counts as a function of time. The histogram represents the temporal distribution of the incoming photons and allows us to extract the fluorescence decay curve and determine the fluorescence lifetime. The peak values observed at 25 ns correspond to the time required for the photons to reach the detector. The areas under the decay curves varied between samples, with a larger area indicating a longer fluorescence lifetime reflecting a slower recombination of excited states. To accurately determine the lifetimes, the instrument response function (IRF) of the system was measured. For this purpose, the Ludox solution was used, which allows a precise calibration of the temporal response of the system. The lifetime (calculated with a multi-exponential fit approach using the Felix FL software) of the TNR support was approximately 0.2 ns, measured at the 350 and 600 nm emissions. A similar measurement was also performed in the study by Santhosa et al. where the average lifetime of TiO_2 was reported to be 0.1 ns [52]. In our case, very similar fluorescence lifetimes were observed for the TNR-PM samples measured at 350 nm (see Table 3 for details). In this case, the samples were excited at 495 nm to activate surface plasmon resonance of the PM. The photogenerated e^- were transferred across the Schottky barrier to the TNR support, where they rapidly recombined with h^+. This fast recombination process, monitored through emission at 350 nm, resulted in a short fluorescence lifetime. However, the lifetime results shown in Table 3 are consistent with the results of the radiative emission (Fig. 6), which show that the longest lifetime (0.18 ns) and the lowest level of photoluminescence were obtained with the TNR-Pt sample. In contrast, TCSPC measurements of TNR-PM samples at 520 nm showed a much broader response attributable to the LSPR effect, and the lifetime apparently extended from 3.9 to 6.85 ns, depending on the PM used. This extended lifetime is probably due to the oscillation of the plasmonic cloud and its influence on the measured data. The actual lifetime,

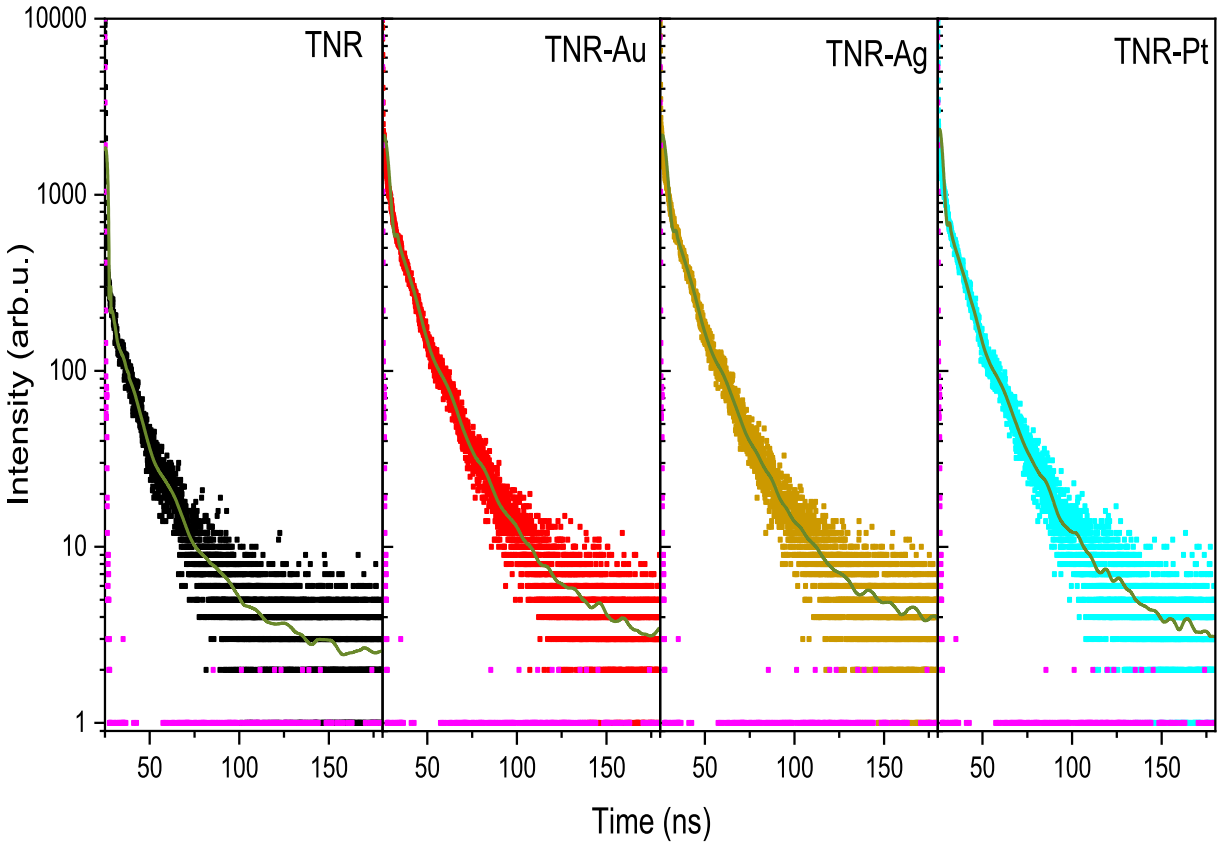

Fig. 7. Time-correlated single photon counting (TCSPC) measurements of the TNR support and TNR-PM catalysts. The purple signal is an IRF response and the green curve represents the exponential fit of the measured signals of the samples. (For interpretation of the references to colour in this figure legend, the reader is referred to the web version of this article.)

Table 3
Results of a fluorescent lifetime and χ^2 value for catalysts obtained by TCSPC analysis.

Sample		TNR	TNR-Au	TNR-Ag	TNR-Pt
Fluorescence lifetime (ns)	$\lambda_{em.}$ = 350 nm	0.26	0.14	0.16	0.18
χ^2 (–)		1.35	1.36	1.24	1.23
Fluorescence lifetime (ns)	$\lambda_{em.}$ = 520 nm	2.81	5.35	3.93	6.85
χ^2 (–)		1.89	1.57	1.62	1.42
Fluorescence lifetime (ns)	$\lambda_{em.}$ = 600 nm	0.20	0.39	0.39	0.38
χ^2 (–)		1.19	1.11	1.09	1.08

measured at 600 nm, is only influenced by the recombination of hot electrons, as the plasmonic cloud has a negligible influence at this wavelength. As mentioned above, spherical Ag nanoparticles typically absorb light at wavelengths around 400–450 nm. However, when they are deposited on a support with a higher refractive index, such as TiO_2, the absorption peak shifts to wavelengths of around 450–500 nm. This shift is due to interactions between the nanoparticles and the substrate, which influence the plasmonic resonance [53]. For this reason, in addition to the emissions for the TNR-Au and TNR-Pt samples, the TCSPC measurements performed with the pulsed laser source at 495 nm also showed emission signals for the TNR-Ag catalyst associated with the recombination of hot e^- at wavelengths up to 600 nm, indicating the gradual decay of the plasmonic wave that disappears at higher wavelengths. For TNR-PM samples, a tailing effect was observed at 520 and 550 nm (Fig. S3), which is characteristic of the prolonged recombination times induced by the plasmonic resonance. In addition, the TNR support itself also prolonged the lifetime measured at 520 nm compared to 350 or 600 nm. This is to be expected since the emission at 520 nm depends primarily on trap-assisted recombination. At 600 nm, the lifetime of the TNR-PM catalysts was extended compared to bare TiO_2. The samples with deposited PM exhibited a longer lifetime (Table 3), confirming that the PM improves the performance of the TNR catalysts by enhancing charge separation and reducing recombination rates, which is also confirmed by solid-state PL measurements (Fig. 6).

For the XPS analysis, measurements were carried out on three different areas of the sample surface. The homogeneous nature of the sample ensured consistent quantitative data across all measurements and confirmed the uniformity of the surface. The survey spectra and high-resolution spectra for Ti 2p, Au 4f, Ag 3d and Pt 4f are shown in Fig. 8. Characteristic peaks for C 1 s, O 1 s, Ti 2p, Ti 3p and Ti 3 s were observed for all samples, with consistent profiles reflecting the uniform composition of the surface. The fitted O 1 s and C 1 s spectra of the TNR catalysts are shown in SI in Fig. S4. A prominent peak of 358.7 eV was observed in all catalysts analyzed, indicating the presence of Ti(IV) throughout. This binding energy is consistent with the literature values [54] for Ti(IV) species, which supports the assignment. Despite the relatively low metal concentration, the PM peaks were clearly visible in the spectra, demonstrating the sensitivity of the XPS technique. The Au $4f_{7/2}$ peak was observed at 83.1 eV, shifted to a lower binding energy compared to bulk Au (83.95 eV). Similarly, the Ag $3d_{5/2}$ peak at 367.6 eV and the Pt $4f_{7/2}$ peak at 70.8 eV were also shifted to lower binding energies compared to bulk Ag (368.2 eV) and bulk Pt (70.98 eV), respectively. These shifts could be due to e^- transfer from the TiO_2 support to the nanoparticles [55,56]. Interestingly, the metallic peaks exhibited different degrees of asymmetry, which could provide information about the electronic environment of the metals. The Pt $4f_{7/2}$ peak was clearly asymmetric, the Ag $3d_{5/2}$ peak showed only slight

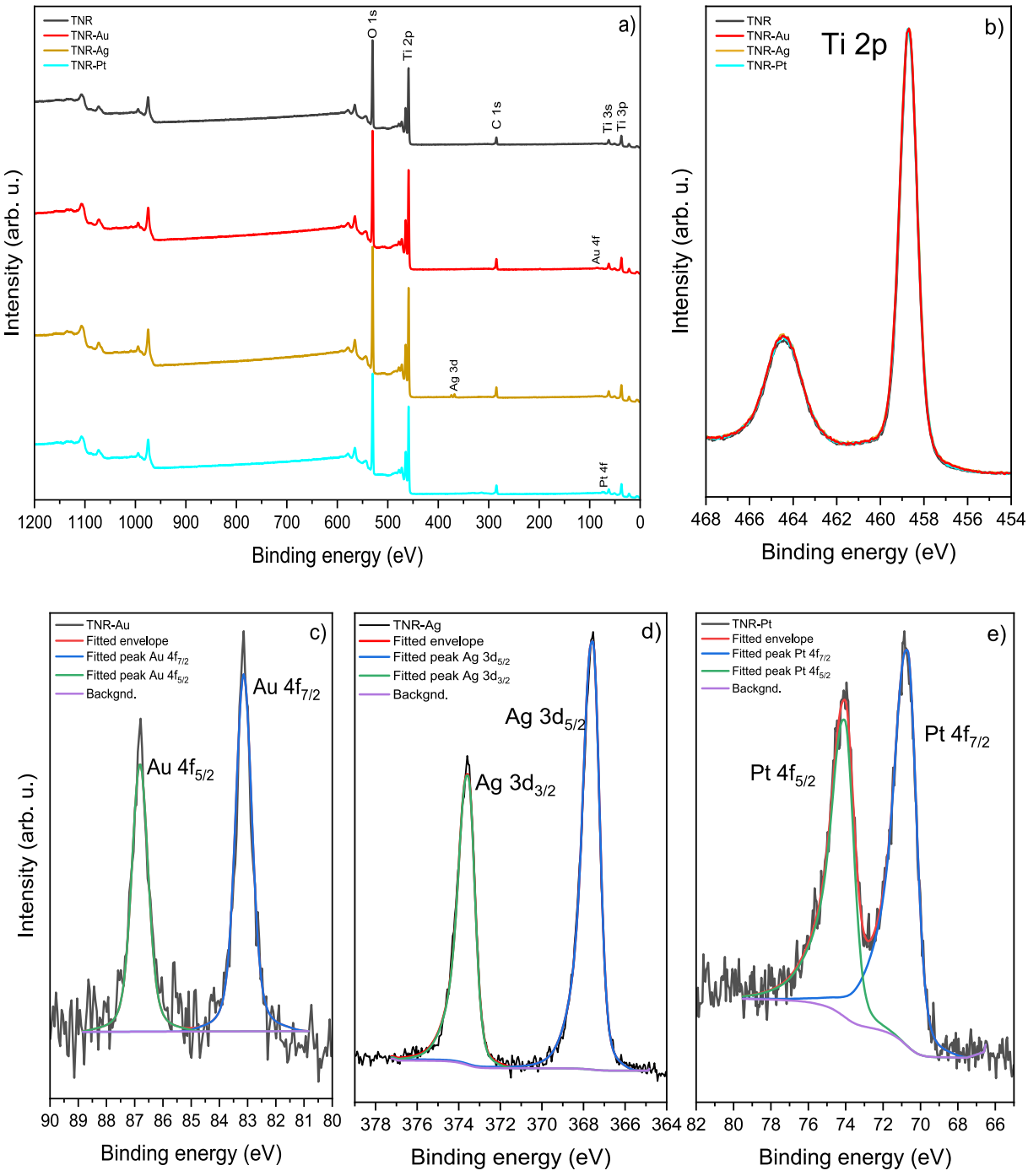

Fig. 8. a) Survey spectra for TNR, TNR-Au, TNR-Ag and TNR-Pt samples and b) high-resolution Ti 2p, c) Au 4f, d) Ag 3d and e) Pt 4f spectra for the analyzed catalysts.

asymmetry, while the Au $4f_{7/2}$ peak appeared symmetric, which is characteristic of bulk metallic Au. The Schottky barrier (SB) forms at the interface between the PM and TiO_2 and influences the transfer of hot charge carriers between the contacted metal and the semiconductor. The SB height (SBH) is calculated as the difference between $\varnothing_M$ and χ [57]. $\varnothing_M$ represents the work function of Au and χ is the e^- affinity of the TNR catalyst. The positions of the valence band maxima (VBM) are shown in Fig. 9, and the calculated SBH values of the investigated samples are listed in Table 1. In principle, a low SBH value is preferable for the transfer of e^- from the plasmonic metal to the TiO_2 support. A high SBH value can lead to an accumulation of e^- at the SB, which increases the probability of their recombination with the hot h^+ generated in the plasmonic metal. This recombination reduces the availability of e^- to generate reactive oxygen species (ROS) or to directly degrade organic pollutants dissolved in water. However, it is important to note that the high SB also hinders e^- transfer from TiO_2 to the PM nanoparticles. The TNR-PM catalysts exhibited SBH values of ~0.1 eV, indicating that SBH had no significant effect on their differential catalytic performance (more details below).

The energy band distribution of the catalysts derived from UV–Vis DR and XPS data is shown in Fig. 9 (inset). For information, the positions of the VB were determined from XPS measurements (VBM), while the band gap energies were derived from UV–Vis DR spectra, and the CB potentials were then calculated as the difference between VBM and band

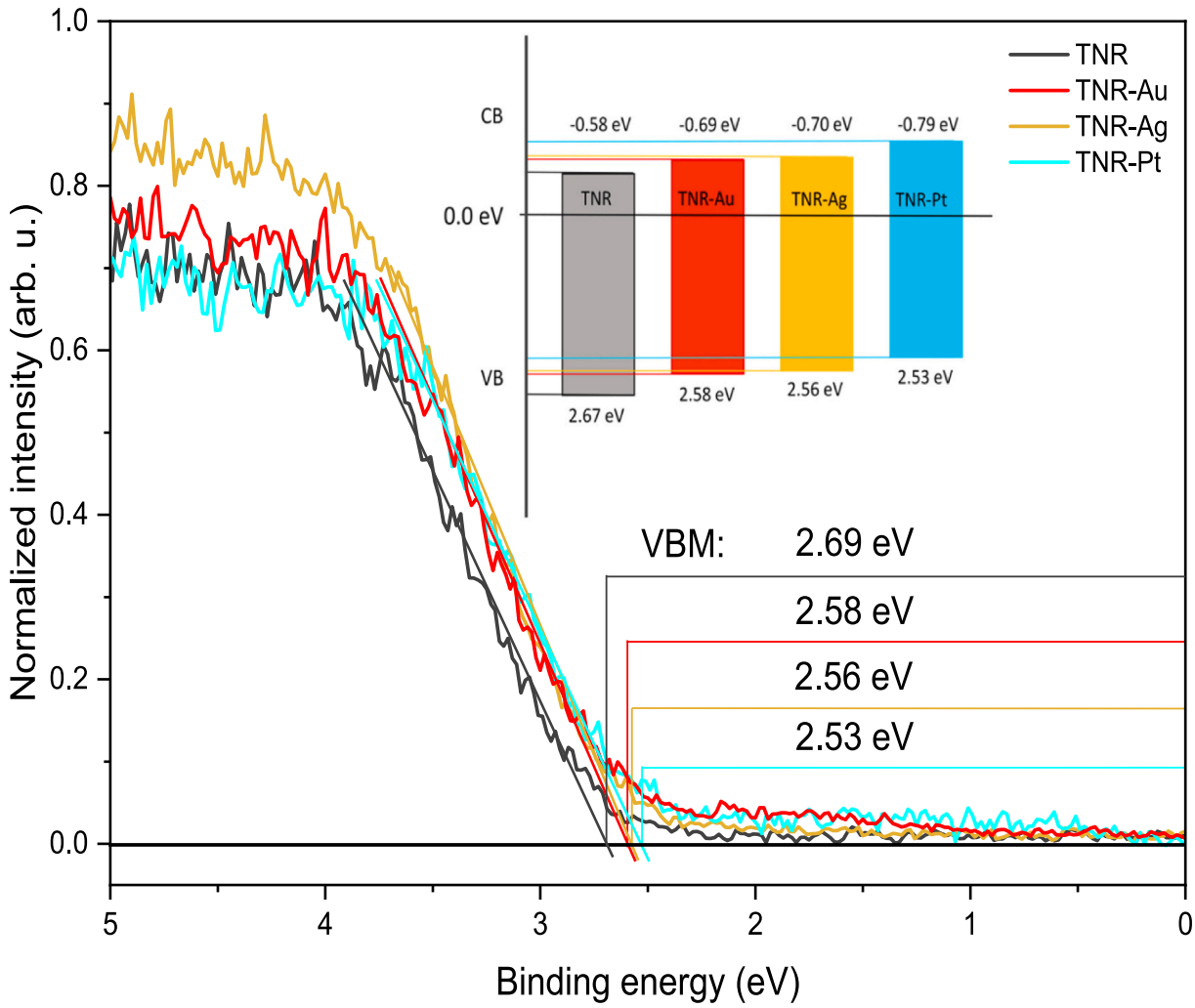

Fig. 9. Determination of the VBM of pure TNR and TNR-PM photocatalysts. The inset shows the energy band distribution for all catalysts.

gap. These results are crucial for understanding the effectiveness of the catalysts. The calculated CB potentials of the catalysts ranged from −0.58 eV to −0.79 eV, while the VB potentials ranged from 2.53 eV to 2.69 eV. The standard reduction potential for the redox pair $O_2/O_2^{\bullet-}$ in aqueous media is −0.16 eV [58,59]. It is known that materials with a CB potential that is more negative than the $O_2/O_2^{\bullet-}$ reduction potential enable a faster oxygen reduction reaction. On this basis and taking into account the facts described above that (i) the radiative emission is lowest for the TNR-Pt sample (Fig. 6) and (ii) the recombination of the generated hot electrons is independent of the plasmonic metal particles deposited on the TiO_2 support (Table 3), we assume that the TNR-Pt catalyst has the highest catalytic activity among the analyzed TNR-PM samples due to its most negative CB potential.

3.3. Photocatalytic activity of the investigated materials

The photocatalytic activity of the investigated materials was first tested for the ability of the materials to generate ROS and charge carriers by illuminating aqueous solutions of DPPH, COUM and $ABTS^{\bullet+}$ containing the investigated materials with visible light. We also tested the photocatalytic activity of the solids with the organic model pollutant bisphenol A (BPA).

3.3.1. Generation of ROS under visible-light exposure

The results of the DPPH reaction test, in which the relative concentration of DPPH was measured at $\lambda = 523$ nm, are shown in Fig. 10a and demonstrate the ability of the investigated TNR-PM catalysts to generate e^-, h^+, superoxide ($O_2^{\bullet-}$) and hydroxyl radicals ($OH^{\bullet}$). The colour of the DPPH and catalyst suspension changed from violet to yellow, which is due to the transition of DPPH to a semi-stable free radical. It can be seen that the fastest degradation of DPPH occurs in the reaction with the TNR-Pt catalyst, where complete degradation occurs in 16 min. In contrast, the slowest DPPH degradation was achieved in the presence of the TNR-Au sample, where the complete degradation of DPPH was five times slower.

The results of the COUM reaction tests shown in Fig. 10b give us an insight into the ability of the catalysts investigated to generate $OH^{\bullet}$ radicals in the presence of TNR-PM photocatalysts under illumination with visible light. The oxidation of COUM by $OH^{\bullet}$ radicals leads to the formation of products, one of which is the fluorescent component 7-OHC. The trend of 7-OHC formation again shows that most $OH^{\bullet}$ radicals were formed in the TNR-Pt sample and the fewest in the TNR-Ag sample. This time the rate of $OH^{\bullet}$ radical formation over the TNR-Au sample was enhanced, which is most likely due to the fact that the Au nanoparticles are larger and consequently have a stronger metallic character. The COUM reaction occurs after the formation of the intermediate H_2O_2, which decomposes most rapidly in the presence of a metal. The larger the metal, the faster $OH^{\bullet}$ radicals are formed via H_2O_2. Some formation of $OH^{\bullet}$ radicals was also observed in the TNR sample, which could be due to the presence of defects on the surface of TiO_2. To directly and accurately confirm the presence of localized surface plasmon resonance effects in an aqueous suspension, the micro-scale

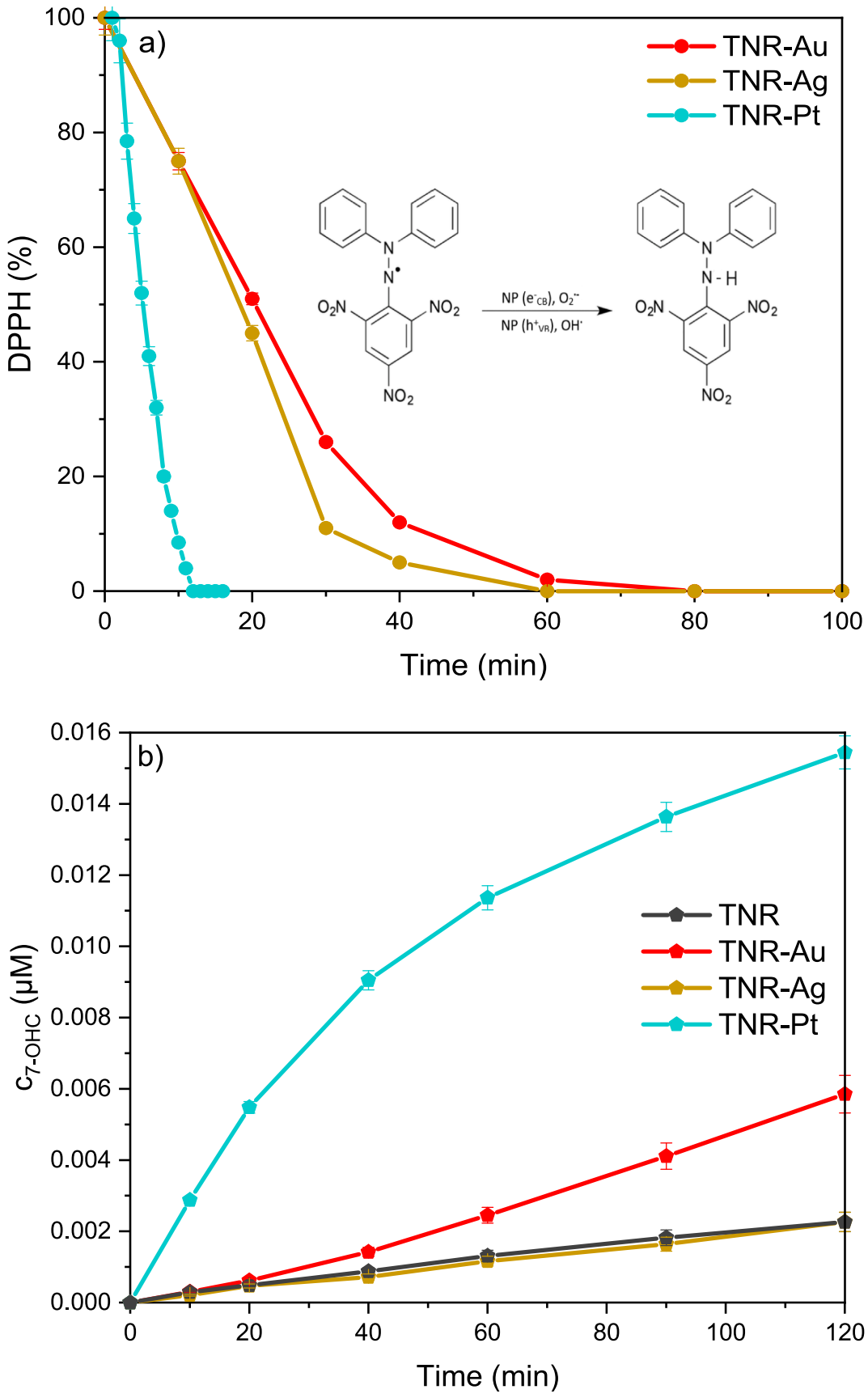

Fig. 10. a) The relative DPPH content as a function of time in the presence of the investigated TNR-PM photocatalysts and b) the relative concentration of 7-hydroxycoumarin (7-OHC) as a function of the illumination time with visible light in the presence of TNR and TNR-PM photocatalysts.

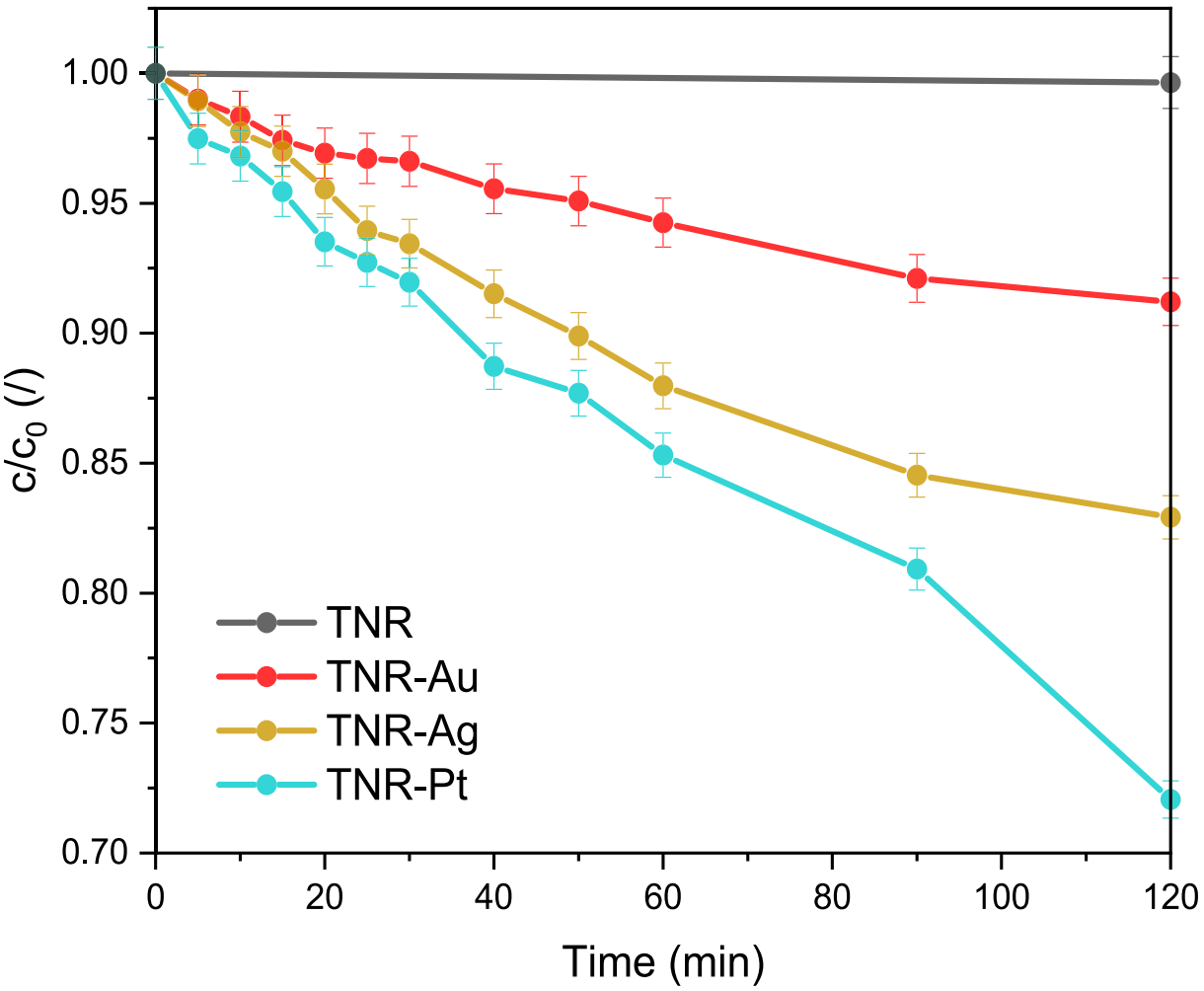

Fig. 11. The relative concentration of the 2,2′-azino-bis-(3-ethylbenzothiazoline-6-sulfonic acid) cation ($ABTS^{\bullet+}$) as a function of visible-light illumination time obtained in the presence of TNR and TNR-PM photocatalysts to monitor the generation of e^- in the conduction band and the formation of superoxide anion radicals $O_2^{\bullet-}$.

reaction was recorded using the COUM probe as a trap for $OH^{\bullet}$ radicals in a UV–Vis spectrophotometer with a well-defined light source. The reaction took place in a cuvette containing 2 mg of the plasmonic catalysts and 3 mL of the COUM solution, with stirring for 24 h. The suspension was illuminated with $\lambda = 550 \pm 2$ nm for all synthesized photocatalysts for the entire duration of the experiment. The results in Fig. S5 show that the plasmonic effects leading to hot electron generation occur in the presence of all TNR-PM samples. As expected, the trend is similar to the reaction with COUM (Fig. 10b), where the concentrations of 7-OHC were higher due to the particularities of the reactor setup. The results thus confirm that the TNR-Pt sample has the highest efficiency in generating $OH^{\bullet}$ radicals.

The monitoring of ROS formed in the $ABTS^{\bullet+}$ reaction was conducted at room temperature in a 50 mL glass reactor illuminated with visible light. During the reaction, the formation of e^- and $O_2^{\bullet-}$ was monitored. From the trends shown in Fig. 11, we can conclude that most e^- and $O_2^{\bullet-}$ were formed in the presence of the TNR-Pt sample and the least over the TNR-Au sample. No formation of $O_2^{\bullet-}$ was observed for the TNR support, which was expected since TNR is not active under visible light. The reaction with $ABTS^{\bullet+}$ confirms that the energy bands play an important role in the oxygen reduction reaction (Fig. 9, inset), as the TNR-Pt sample with the most negative CB potential showed the largest formation of $O_2^{\bullet-}$.

In the TNR-Pt sample, the recombination of the e^--h^+ pairs are the slowest, which is confirmed by the lifetime measurements (Figs. 6 and 7, Table 3). Consequently, this sample also exhibits the highest formation of ROS. In comparison, differences in the lifetimes and recombination rates were observed in the TNR-Au and TNR-Ag samples, with recombination occurring faster in the TNR-Ag sample. Due to the faster recombination, the utilization of h^+ is limited, which leads to a lower formation of $OH^{\bullet}$ radicals compared to the TNR-Au sample. On the other hand, the formation of $O_2^{\bullet-}$ radicals is more pronounced in the TNR-Ag sample because Ag more readily donates e^- to the conduction band of TiO_2, which promotes the oxygen reduction reaction and the formation of $O_2^{\bullet-}$ radicals.

In our recent study [60], it was reported that the formation of $O_2^{\bullet-}$ radicals in the presence of plasmonic Au/TiO_2 catalysts illuminated with visible light strongly depends on the electronic properties of the materials. In particular, it has been experimentally demonstrated that the oxygen reduction reaction (ORR) cannot take place if the Schottky barrier is too high, as the photogenerated hot electrons cannot be efficiently transferred to the conduction band of TiO_2, where the ORR takes place. However, if the Schottky barrier is sufficiently low, as is the case for the TNR-PM catalysts investigated in this study, electron transfer is no longer restricted by the interface. Instead, the formation of $O_2^{\bullet-}$ radicals is primarily determined by the conduction band potential of the photocatalysts. Of the materials investigated, the TNR-Pt catalyst exhibits the most favourable CB position for oxygen reduction and enables more efficient e^- transfer than the TNR-Ag and TNR-Au samples. This indicates that, in addition to the Schottky barrier effect, the energetic orientation of the conduction band also plays a decisive role in determining the photocatalytic activity.

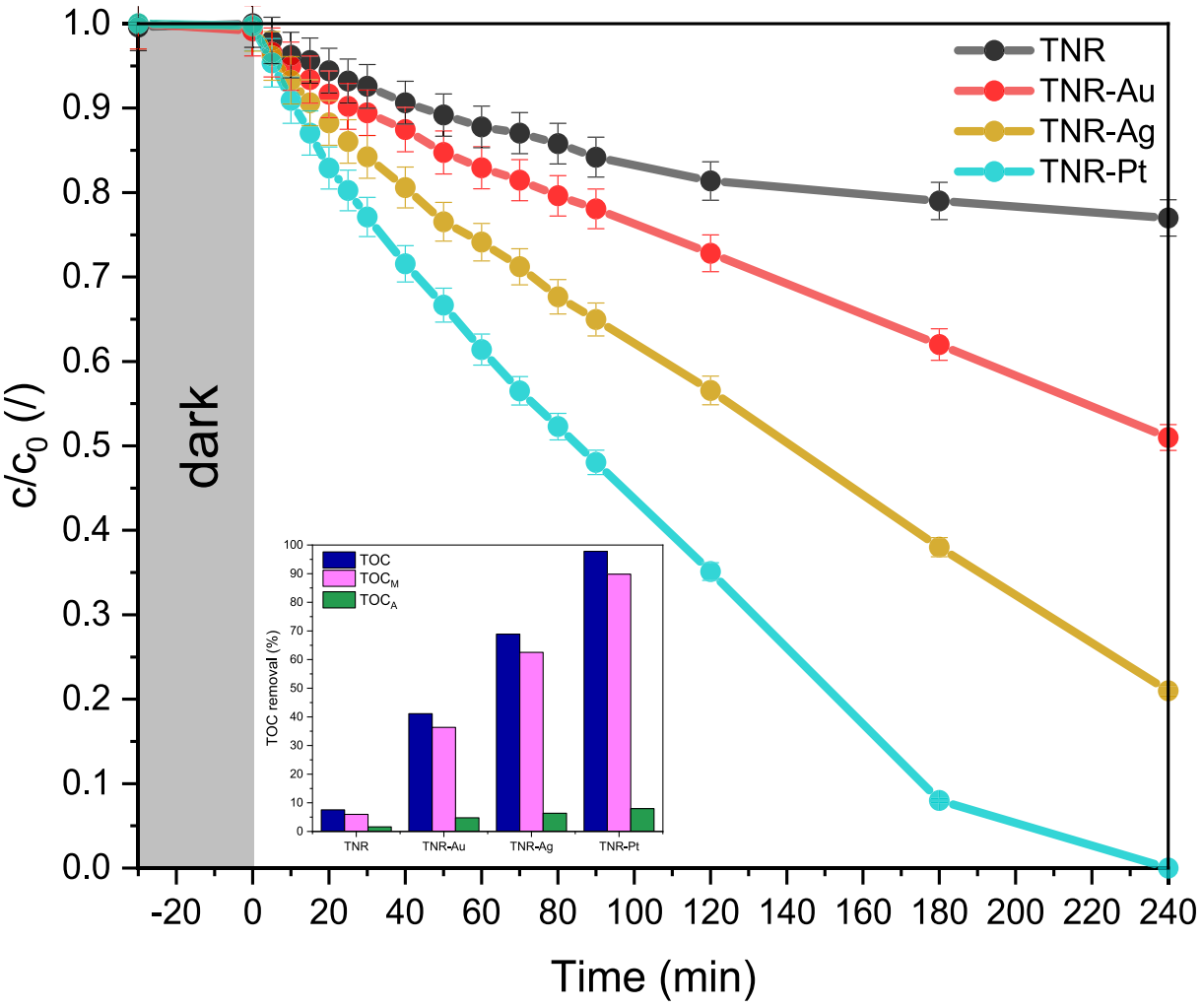

Fig. 12. Photocatalytic degradation of BPA dissolved in water ($V = 250$ mL, $c_0 = 10.00$ mg/L) under visible-light illumination at $T = 25$ °C in the presence of pure TNR support and TNR-PM catalysts (125 mg/L). The inset shows the results of total organic carbon (TOC) removal - a sum of TOC mineralization (TOC_M) and TOC accumulation (TOC_A) - measured at the end of the degradation runs.

Table 4
Comparison of pollutant degradation with TiO_2 based materials.

Sample	Pollutant degradation	Pollutant initial concentration (mg/L)	Catalyst concentration (mg/L)	Metal loading (wt%)	Metal particle size (nm)	Main oxidizing species	Reference
TiO_2/UV-C	98 % of BPA in 120 min under UV	5.0	120	–	–	$OH^•$	[61]
Au/P25	80–83 % of BPA in 24 h under Vis	66.8	1000	0.3–0.7	11–14	No info	[62]
TiO_2-Au/ IWI	50 % of 2,4 DNP in 120 min under UV	20.0	1000	1.0	No info	No info	[63]
Ag-TiO_2 NPs	94.42 % of BPA in 180 min under Vis	10.0	2000	No info	No info	$OH^•$ and $O_2^{•-}$	[28]
Ag@TiO_2	95.8 % of BPA in 110 min under Vis	5.0	200	2.0	Different sizes	h^+	[64]
SA-Pt/TiO_2	70 % of DMMP in 120 min under Vis	80.0	1500	1.0	No info	$OH^•$ and $O_2^{•-}$	[29]
TNP + Pt	100 % of BPA in 80 min under Vis	10.0	125	1.0	5–7	No info	[65]
TNR-Au	50 % of BPA in 240 min under Vis	10.0	125	1.0	45	$O_2^{•-}$	This study
TNR-Ag	80 % of BPA in 240 min under Vis	10.0	125	1.0	5	$O_2^{•-}$	This study
TNR-Pt	100 % of BPA in 240 min under Vis	10.0	125	1.0	1.5	$O_2^{•-}$	This study

Table 5
Results of carbon elemental analysis for the catalysts TNR and TNR-PM catalysts. TC_{fresh} stands for the carbon value before and TC_{spent} for the carbon value after the reaction to degrade the BPA pollutants.

Sample		TNR	TNR-Au	TNR-Ag	TNR-Pt
TC_{fresh}	%	0.5	0.4	0.5	0.7
TC_{spent}		0.6	0.7	0.9	1.1
TOC		7.56	41.11	68.89	97.78
TOC_M		5.96	36.34	62.52	89.81
TOC_A		1.6	4.77	6.37	7.97

3.3.2. *Photocatalytic oxidation of BPA dissolved in water*

The results of the degradation of the water-dissolved pollutant BPA carried out in the presence of the synthesized catalysts are shown in Fig. 12. Under the given operating and reaction conditions, no disappearance of BPA in the photolysis run and no adsorption of BPA in the dark phase (grey area) of any of the tested materials was observed. The photocatalytic activity of the bare TNR support can be attributed to the presence of Ti^{3+} species on the surface or to the surface defects. The TNR-Pt catalyst exhibited the highest activity and achieved complete degradation of BPA within 4 h of visible-light illumination, which is consistent with the results of ROS formation. The TNR-Ag sample achieved almost 80 % degradation after 4 h of visible-light exposure, while the efficiency of the TNR-Au sample for BPA disappearance was 50 %. In such a short time span, the tendency of the reactions and the differences between the efficiencies of the individual samples can still be clearly recognized. In agreement with the comments above, the rate and efficiency of photocatalytic BPA degradation were most likely not influenced by the SBH, as all SBHs measured (Table 1) were almost identical. The TNR-Pt catalyst, which is the most active solid for BPA degradation, was also able to produce the largest amount of oxidants for wastewater treatment, as shown by the results of ROS formation (Figs. 10 and 11). TEM analysis showed that the smallest metal Pt particles were deposited on the TNR support, which contributed to a better activity of the TNR-Pt material compared to the TNR-Ag and TNR-Au samples. We have prepared a comparative Table 4 that clearly shows the properties of our material in comparison with previously published studies with similar materials. The table shows that our material achieves very high efficiency even at much lower concentrations used in pollutant degradation reactions.

Finally, Fig. 12 (inset) shows the TOC removal data after completion of the BPA oxidation reaction (i.e. at $t = 240$ min). It can be seen that the TOC results obtained are comparable to the BPA degradation trends. Table 5 shows the results of the carbon elemental analysis for the analyzed catalysts before and after the BPA degradation reaction. Based on the elemental analysis results, we calculated the TOC mineralization (TOC_M) and TOC accumulation (TOC_A) values. The degree of mineralization is lower in all samples compared to the degradation trend of the pollutant BPA, but TOC_M accounts for most of the total TOC, which is satisfactory.

4. Conclusions

The aim of the study presented here was to investigate the influence of different PM, namely Au, Ag and Pt, on the chemical, optoelectronic, structural and photocatalytic properties of the TiO_2-PM catalysts (TiO_2 was present in the form of TNR), where the plasmonic metals were deposited by the same wet impregnation technique regardless of the plasmonic metal used. The results of the SEM-EDXS analysis showed that the actual loading of the PM was about 1.0 wt%, which corresponds to the nominal loading. The average particle size of the deposited plasmonic metals varied depending on the type of plasmonic metal, with the smallest diameter occurring for the Pt particles (1.5 nm) and the largest for Au (45 nm), although all plasmonic metals analyzed showed good uniform distribution on the TNR surface. The different sizes of the metal particles also correlated with the pH values of the precursor solutions and the IEP of the TNR. The fluorescence lifetime was extended by the addition of PM on the TNR support, which improved the catalytic properties, consistent with the solid-state PL measurements that showed lower carrier recombination rates on the TNR-PM samples. However, the TNR-Pt samples showed the lowest recombination rates. The COUM reaction, performed in a cuvette illuminated at 550 nm, confirmed the ability of the TNR-PM catalysts investigated to generate ROS through plasmonic properties and the plasmonic effect of the PM used. The ROS formation tests also confirmed the ability of the investigated TNR-PM catalysts to generate charge carriers, i.e. $O_2^{\bullet-}$ and $OH^{\bullet}$, when illuminated with visible light. The TNR-Au sample showed the lowest charge carrier generation and BPA conversion rate. In contrast, the TNR-Pt sample with the smallest plasmonic nanoparticles showed the highest formation rates of $O_2^{\bullet-}$ and $OH^{\bullet}$ radicals and also the highest BPA degradation rate. The reason for the high formation of $O_2^{\bullet-}$ radicals in the TNR-Pt sample lies in the arrangement of the energy bands, while the SBH has no significant influence as it was the same for all three photocatalysts with PM. From the results of ROS formation and photocatalytic oxidation tests, we conclude that $O_2^{\bullet-}$ radicals are the primary ROS responsible for the oxidation pathway and degradation of the model organic pollutant BPA on the surface of the investigated TNR-PM catalysts. In summary, the most active TNR-PM solid is the Pt catalyst, which has the smallest particles on the catalyst surface, the most favourable energy band distribution and consequently forms more ROS, leading to a very successful degradation of BPA. Importantly, all TNR-PM catalysts maintained their photocatalytic performance over three consecutive degradation cycles without any significant decrease in activity. This confirms their excellent stability and recyclability, which is particularly important for real-world applications. Pt is more expensive, but its outstanding efficiency and proven reusability make it a promising candidate for practical wastewater treatment.

CRediT authorship contribution statement

Špela Slapničar: Writing – review & editing, Writing – original draft, Visualization, Methodology, Investigation. **Gregor Žerjav:** Writing – review & editing, Visualization, Investigation. **Miklós Németh:** Writing – review & editing, Visualization, Investigation. **Janez Zavašnik:** Writing – review & editing, Visualization, Investigation. **Albin Pintar:** Writing – review & editing, Visualization, Supervision, Project administration, Investigation, Funding acquisition.

Declaration of competing interest

The authors declare that they have no known competing financial interests or personal relationships that could have appeared to influence the work reported in this paper.

Acknowledgments

The authors acknowledge the financial support from the Slovenian Research and Innovation Agency (research core funding No. P2-0150).

Appendix A. Supplementary data

Supplementary data to this article can be found online at https://doi.org/10.1016/j.jcis.2025.138361.

Data availability

Data will be made available on request.

References

[1] P.V.L. Reddy, K.-H. Kim, B. Kavitha, V. Kumar, N. Raza, S. Kalagara, Photocatalytic degradation of bisphenol A in aqueous media: a review, J. Environ. Manag. 213 (2018) 189–205.

[2] A. Gupta, A. Singh, V.K. Mishra, Impact of bisphenol-A in the environment and its removal through biological agents: a review, Environ. Qual. Manag. 34 (2024) e22246.

[3] S. Liu, S. Liu, L. Liu, L. Li, Y. Yang, Y. Xu, X. She, Photodegradation of bisphenol A (BPA) in coastal aquaculture waters: influencing factors, products, and pathways, Chemosphere 363 (2024) 142708.

[4] L.N. Vandenberg, Exposure to bisphenol A in Canada: invoking the precautionary principle, Can. Med. Assoc. J. 183 (2011) 1265–1270.

[5] S.A. Hafezi, W.M. Abdel-Rahman, The endocrine disruptor bisphenol A (BPA) exerts a wide range of effects in carcinogenesis and response to therapy, Curr. Mol. Pharmacol. 12 (2019) 230–238.

[6] R. Bahmani, D. Kim, M. Modareszadeh, S. Hwang, Ethylene and ROS mediate root growth inhibition induced by the endocrine disruptor bisphenol A (BPA), Plant Physiol. Biochem. 205 (2023) 108212.

[7] Z. Lin, L. Wang, Y. Jia, Y. Zhang, Q. Dong, C. Huang, A study on environmental bisphenol a pollution in plastics industry areas, Water Air Soil Pollut. 228 (2017) 1–9.

[8] N.R. Maddela, D. Kakarla, K. Venkateswarlu, M. Megharaj, Additives of plastics: entry into the environment and potential risks to human and ecological health, J. Environ. Manag. 348 (2023) 119364.

[9] F.S. vom Saal, C. Hughes, An extensive new literature concerning low-dose effects of bisphenol a shows the need for a new risk assessment, Environ. Health Perspect. 113 (2005) 926–933.

[10] C. Swansborough, J. Soto, I. Shapland, C.B. Hughes, E. Jennings, M. McArdle, E. Mihaich, E. Majoris, M. Bunge, Trend analysis of environmental concentrations of Bisphenol A in European waters and sediments, Environ. Res. 282 (2025) 121946.

[11] L. Tappert, M. Bunge, D. Hoehne, I. Dlugi, K. Fetters, B. Fischer, G. Mueller, M. Bock, S. Gestermann, Bisphenol A in surface waters in Germany: Part I. Reassessment of sources and emissions pathways for FlowEQ modelling, Integr. Environ. Assess. Manag. 20 (2024) 211–225.

[12] T. Yamamoto, A. Yasuhara, Quantities of bisphenol A leached from plastic waste samples, Chemosphere 38 (1999) 2569–2576.

[13] J.R. Masoner, D.W. Kolpin, E.T. Furlong, I.M. Cozzarelli, J.L. Gray, Landfill leachate as a mirror of today's disposable society: pharmaceuticals and other contaminants of emerging concern in final leachate from landfills in the conterminous United States, Environ. Toxicol. Chem. 35 (2016) 906–918.

[14] U. Hübner, S. Spahr, H. Lutze, A. Wieland, S. Rüting, W. Gernjak, J. Wenk, Advanced oxidation processes for water and wastewater treatment – guidance for systematic future research, Heliyon 10 (2024) e30402.

[15] M.A. Oturan, J.-J. Aaron, Advanced oxidation processes in water/wastewater treatment: principles and applications. A review, Crit. Rev. Environ. Sci. Technol. 44 (2014) 2577–2641.

[16] Y. Deng, R. Zhao, Advanced oxidation processes (AOPs) in wastewater treatment, Curr. Pollut. Rep. 1 (2015) 167–176.

[17] A. Chakravorty, S. Roy, A review of photocatalysis, basic principles, processes, and materials, Sustain. Chem. Environ. 8 (2024) 100155.

[18] Y. Huang, X. Xu, G. Fan, X. Zhu, L. Zhu, X. Chen, Effect of TiO_2 crystal phase on the construction of TiO_2/g-C_3N_4 heterojunction photocatalyst for efficient sunlight photodegradation of naphthalene, Colloids Surf. A Physicochem. Eng. Asp. 694 (2024) 134170.

[19] A. Kumar, P. Choudhary, A. Kumar, P.H.C. Camarago, V. Krishnan, Recent advances in plasmonic photocatalysis based on TiO_2 and noble metal nanoparticles for energy conversion, environmental remediation, and organic synthesis, Small 18 (2022) 2101638.

[20] R. Amrollahi, M.S. Hamdy, G. Mul, Understanding promotion of photocatalytic activity of TiO_2 by Au nanoparticles, J. Catal. 319 (2014) 194–199.

[21] I. Hammami, N.M. Alabdallah, A. Al Jomaa, Gold nanoparticles: synthesis properties and applications, J. King Saud Univ. Sci. 33 (2021) 101560.

[22] D.T. Thompson, Using gold nanoparticles for catalysis, Nano Today 2 (2007) 40–43.

[23] N.H. Ramli, N.M. Nor, A.H.A. Bakar, N.D. Zakaria, Z. Lockman, K.A. Razak, Platinum-based nanoparticles: a review of synthesis methods, surface functionalization, and their applications, Microchem. J. 200 (2024) 110280.

[24] A. Meher, A. Tandi, S. Moharana, S. Chakroborty, S.S. Mohapatra, A. Mondal, S. Dey, P. Chandra, Silver nanoparticle for biomedical applications: a review, Hybrid Adv. 6 (2024) 100184.

[25] K.-S. Kim, D. Demberelnyamba, H. Lee, Size-selective synthesis of gold and platinum nanoparticles using novel thiol-functionalized ionic liquids, Langmuir 20 (2004) 556–560.

[26] K.D. Rasamani, Y. Sun, Promoting reactivity of photoexcited hot electrons in small-sized plasmonic metal nanoparticles that are supported on dielectric nanospheres, J. Chem. Phys. 152 (2020) 084706.

[27] J. Zhu, J. Huang, J. Dai, R. Chen, X. Fu, Z. Wang, H. Liu, G. Li, Size effect on formic acid dehydrogenation over Plasmonic Au@Pd Core-satellite nanostructures, ACS Appl. Energy Mater. 5 (2022) 10013–10022.

[28] R. Hidayat, G. Fadillah, S.-I. Ohira, F.I. Fajarwati, D.A. Setyorini, A. Saputra, Facile green synthesis of Ag doped TiO_2 nanoparticles using maple leaf for bisphenol-A degradation and its antibacterial properties, Mater. Today Sustain. 26 (2024) 100752.

[29] C.-S. Cao, W. Liu, A. Ma, X. Jiao, Y. Yang, J. Li, F. Fu, Single-atom Pt-decorated TiO_2 nanotubes for boosted photocatalytic degradation of chemical warfare agents, ACS Sustain. Chem. Eng. 13 (2025) 6379–6387.

[30] G. Žerjav, M.S. Arshad, P. Djinović, J. Zavašnik, A. Pintar, Electron trapping energy states of TiO_2-WO_3 composites and their influence on photocatalytic degradation of bisphenol A, Appl Catal B 209 (2017) 273–284.

[31] Š. Slapničar, G. Žerjav, J. Zavašnik, M. Finšgar, A. Pintar, Synthesis and characterization of plasmonic Au/TiO_2 nanorod solids for heterogeneous photocatalysis, J. Environ. Chem. Eng. 11 (2023) 109835.

[32] P. Verma, K. Mori, Y. Kuwahara, S. June Cho, H. Yamashita, Synthesis of plasmonic gold nnaoparticles supported on morphology-controlled TiO_2 for aerobic alcohol oxidation, Catal. Today 352 (2020) 255–261.

[33] G. Louit, S. Foley, J. Cabillic, H. Coffigny, F. Taran, A. Valleix, J.P. Renault, S. Pin, The reaction of coumarin with the OH radical revisted: hydroxylation product analysis determined by flourescence and chromatography, Radiat. Phys. Chem. 72 (2005) 119–124.

[34] E.N. Hristea, M. Hillebrand, M.T. Caproiu, H. Caldararu, T. Constantinescu, A. T. Balaban, Scavenging the hydroxyl radical by 2,2-diphenyl-1-picrylhydrazyl, Arkivoc (2002) 123–132.

[35] M.C. Foti, Use and abuse of the DPPH(•) radical, J. Agric. Food Chem. 63 (2015) 8765–8776.

[36] V. Brezová, D. Dvoranová, A. Staško, Characterization of titanium dioxide photoactivity following the formation of radicals by EPR spectroscopy, Res. Chem. Intermed. 33 (2007) 251–268.

[37] R. Isono, T. Yoshimura, K. Esumi, Preparation of Au/TiO_2 nanocomposites and their catalytic activity for DPPH radical scavenging reaction, J. Colloid Interface Sci. 288 (2005) 177–183.

[38] M.I. Zaki, N.E. Fouad, G.A.H. Mekhemer, T.C. Jagadale, S.B. Ogale, TiO_2 nanoparticle size dependence of porosity, adsorption and catalytic activity, Colloids Surf. A: Physicochem. Eng. Aspects 385 (2011) 195–200.

[39] F.J. Sotomayor, K.A. Cychosz, M. Thommes, Characterization of micro/mesoporous materials by physisorption: concepts and case studies, Acc. Mater. Surf. Res. 3 (2018) 34–50.

[40] P. Bertier, K. Schweinar, H. Stanjek, A. Ghanizadeh, C.R. Clarkson, A. Busch, N. Kampman, D. Prinz, A. Amann-Hildenbrand, B.M. Krooss, V. Pipich, On the use and abuse of N_2 physisorption for the characterization of the pore structure of shales, CMS Workshop Lectures 21 (2016) 151–161.

[41] C.F. Holder, R.E. Schaak, Tutorial on powder X-ray diffraction for characterizing nanoscale materials, ACS Nano 13 (2019) 7359–7365.

[42] X. Tan, S. Shahgaldi, X. Li, The effect of non-spherical platinum nanoparticle sizes on the performance and durability of proton exchange membrane fuel cells, Adv. Appl. Energy 4 (2021) 100071.

[43] M.A.R. Khan, M.S. Al Mamun, M.H. Ara, Review on platinum nanoparticles: synthesis, characterization, and applications, Microchem. J. 171 (2021) 106840.

[44] H. Yazid, R. Adnan, M.A. Farrukh, Gold nanoparticles supported on titania for the reduction of *p*-nitrophenol, Indian J. Chem. 52 (2013) 184–191.

[45] R. Zanella, S. Giorgio, C.R. Henry, C. Louis, Alternative methods for the preparation of gold nanoparticles supported on TiO_2, J. Phys. Chem. B 106 (2002) 7634–7642.

[46] S. Agnihotri, S. Mukherji, S. Mukherji, Size-controlled silver nanoparticles synthesized over the range 5-100 nm using the same protocol and their antibacterial efficacy, RSC Adv. 4 (2014) 3974–3983.

[47] U. Aslam, V.G. Rao, S. Chavez, S. Linic, Catalytic conversion of solar to chemical energy on plasmonic metal nanostructures, Nat. Catal. 1 (2018) 656–665.

[48] C. Dette, M.A. Pérez-Osorio, C.S. Kley, P. Punke, C.E. Patrick, P. Jacobson, F. Giustino, S.J. Jung, K. Kern, TiO_2 Anatase with a bandgap in the visible region, Nano Lett. 14 (2014) 6533–6538.

[49] K.M. Reddy, S.V. Manorama, A.R. Reddy, Bandgap studies on anatase titanium dioxide nanoparticles, Mater. Chem. Phys. 78 (2003) 239–245.

[50] V. Jovic, Z.H.N. Al-Azri, W.T. Chen, D. Sun-Waterhouse, H. Idriss, G.I. N. Waterhouse, Photocatalytic H_2 production from ethanol-water mixtures over Pt/TiO_2 and Au/TiO_2 Photocatalysts: a comparative study, Top. Catal. 56 (2013) 1139–1151.

[51] H. Nakajima, T. Mori, M. Watanabe, Influence of platinum loading on photoluminiscence of TiO_2 powder, J. Appl. Phys. 96 (2004) 925–927.

[52] K. Santhosh, S. Sk, S. Chouti, S. Gonuguntla, S.P. Ega, A. Tiwari, U. Pal, Tailoring hierarchical porous TiO_2 based ternary rGO/NiO/TiO_2 photocatalyst for efficient hydrogen production and degradation of Rhodamine B, J. Mol. Struct. 1235 (2021) 130222.

[53] D. Thomas, E. Danladi, M.T. Ekwu, P.M. Gyuk, M.O. Abdulmalik, I.O. Echi, Effect of silver nanoparticles SILAR cycle on TiO_2 nanoparticles thin film: optical and structural study, East Eur. J. Phys. 4 (2022) 118–124.

[54] M.C. Biesinger, L.W.M. Lau, A.R. Gerson, R.St.C. Smart, Resolving surface chemical states in XPS analysis of first row transition metals, oxides and hydroxides: Sc, Ti, V, Cu and Zn, Appl. Surf. Sci. 257 (2010) 887–898.

[55] M. Sankar, Q. He, M. Morad, J. Pritchard, S.J. Freakley, J.K. Edwards, S.H. Taylor, D.J. Morgan, A.F. Carley, D.W. Knight, C.J. Kiely, G.J. Hutchings, Synthesis of stable ligand-free gold-palladium nanoparticles using a simple excess anion method, ACS Nano 6 (2012) 6600–6613.

[56] M.-J. Choi, H. Park, M.H. Engelhard, D. Li, P.V. Sushko, Y. Du, Reevaluation of XPS Pt 4f peak fitting: Ti 3s plasmon peak interference and Pt metallic peak asymmetry in Pt@TiO_2 system, J. Vac. Sci. Technol. A 42 (2024) 063209.

[57] Z. Zhang, J.T. Yates, Band bending in semiconductors: chemical and physical consequences at surfaces and interfaces, Chem. Rev. 112 (2012) 5520–5551.

[58] W. He, H. Jia, D. Yang, P. Xiao, X. Fan, Z. Zheng, H.-K. Kim, W.G. Wamer, J.-J. Yin, Composition directed generation of reactive oxygen species in irradiated mixed

metal sulfides correlated with their photocatalytic activities, ACS Appl. Mater. Interfaces 7 (2015) 16440–16449.
[59] P.M. Wood, The potential diagram for oxygen at pH 7, Biochem. J. 253 (1988) 287–289.
[60] Š. Slapničar, G. Žerjav, M. Roškarič, J. Zavašnik, A. Pintar, Variations of electronic properties on the behaviour of visible light-triggered TiO_2+Au photocatalysts, Appl. Surf. Sci. 695 (2025) 162923.
[61] J.C.C. da Silva, J.A.R. Teodoro, R.J.C.F. Afonso, S.F. Aquino, R. Augusti, Photodegradation of bisphenol A in aqueous medium: monitoring and identification of by-products by liquid chromatography coupled to high-resolution mass spectrometry, Rapid Commun. Mass Spectrom. 28 (2014) 987–994.
[62] B. Cojocaru, V. Andrei, M. Tudorache, F. Lin, C. Cadigan, R. Richards, V. I. Parvulescu, Enhanced photo-degradation of bisphenol pollutants onto gold-modified photocatalysts, Catal. Today 285 (2017) 153–159.
[63] A.M. Sescu, L. Favier, D. Lutic, N. Soto-Donoso, G. Ciobanu, M. Harja, TiO_2 doped with Noble metals as an efficient solution for the photodegradation of hazardous organic water pollutants at ambient conditions, Water 13 (2020) 19.
[64] S. Sambaza, A. Maity, K. Pillay, Enhanced degradation of BPA in water by PANI supported Ag/TiO_2 nanocomposite under UV and visible light, J. Environ. Chem. Eng. 7 (2019) 102880.
[65] G. Žerjav, Z. Say, J. Zavašnik, M. Finšgar, C. Langhammer, A. Pintar, Photo, thermal and photothermal activity of TiO_2 supported Pt catalysts for plasmon-driven environmental applications, J. Environ. Chem. Eng. 11 (2023) 110209.